Assessment of time-series-derived no-flood references for sar-based Bayesian flood mapping

Mark Edwin Tupas, Florian Roth, Bernhard Bauer-Marschallinger & Wolfgang Wagner

View supplementary material ☐

Published online: 01 Dec 2024.

Submit your article to this journal ☐

Article views: 265

View related articles ☐

View Crossmark data ☐

Taylor & Francis
Taylor & Francis Group

🔓 OPEN ACCESS | Check for updates

Assessment of time-series-derived no-flood references for sar-based Bayesian flood mapping

Mark Edwin Tupas [a,b], Florian Roth [a], Bernhard Bauer-Marschallinger [a] and Wolfgang Wagner [a,c]

aRemote Sensing Research Group, Department of Geodesy and Geoinformation, TU Wien, Vienna, Austria; bDepartment of Geodetic Engineering, University of the Philippines Diliman, Quezon, Philippines; cEODC Earth Observation Data Centre for Water Resources Monitoring, Vienna, Austria

ABSTRACT

The systematic mapping of flood events with Synthetic Aperture Radar (SAR) data is an area of growing importance. One global flood mapping algorithm utilized within the Copernicus Emergency Management Service is based upon a Bayesian Inference model that compares a SAR image to a simulated reference image representing no-flood conditions. This no-flood reference image is at present generated using a harmonic model trained using historic time series, thereby producing a backscatter image representing mean seasonal conditions. One known weakness of this approach is that it cannot account for changing environmental conditions from year to year, potentially causing an overestimation of flood extent during dry periods, snow and frost, or other effects causing lower-than normal backscatter. To minimize this detrimental effect, we introduce an exponential filter to estimate the no-flood reference image by weighting the most recent backscatter observations according to their time difference to the current SAR acquisition. We compare the performance of the new exponential filter model against the harmonic model using a novel time-series flood mapping assessment approach. First, we assess their predictions against the actual SAR image time series for the year 2023. Then, we analyze the false positive rate of the corresponding flood maps generated to ensure the robustness of the automated algorithm outside of flood events. Furthermore, we perform qualitative and quantitative analyses of flood maps matching with semi-automatic results from Copernicus Emergency Management Services and Sentinel Asia as a reference. Our time-series analysis confirms increased false positive rates due to well-known environmental drivers and highlights issues with agricultural overestimation. In this regard, the time-series comparisons of the no-flood reference models show a clear improvement in the TU Wien algorithm with the exponential filter, effectively reducing false positive rates on non-flooded scenes in most study sites. The exponential filter performed better than the harmonic model in most flooded scenes, where sites show generally improved Critical Success Index and User's accuracy. However, the exponential filter model has difficulties with sites with prolonged floods in the time series, requiring further development. Overall, the exponential filter no-flood reference model shows great promise for improved global near-real-time flood mapping.

1. Introduction

Floods are among the most frequent natural disasters affecting an increasing segment of the global population (Ceola, Laio, and Montanari 2014; Tellman et al. 2021). A recent estimate suggests that 1.81 billion people, or almost one in four persons are directly exposed to severe flooding (Rentschler, Salhab, and Jafino 2022). Using remote sensing for large-scale mapping of flood situations is invaluable for emergency response, recovery, and reconstruction. Supporting these applications, Synthetic Aperture Radar (SAR) based flood mapping is gaining prominence for systematic global operations due to its spatiotemporal coverage and independence from weather and ligthining conditions (Salamon et al. 2021; Schumann et al. 2023; Tarpanelli, Mondini, and Camici 2022).

SAR-based flood mapping techniques that have proven effective include single-image thresholding algorithms (Grimaldi et al. 2020; Martinis, Twele, and Voigt 2009), parametric or tile-based thresholding schemes (Chini et al. 2017; Martinis, Kersten, and Twele 2015; Twele et al. 2016; Zhao, Pelich,

Hostache, Matgen, Wagner, et al. 2021), and machine learning methods (Katiyar, Tamkuan, and Nagai 2021; Shen et al. 2019; Wu et al. 2023). However, due to floods' transient and anomalous nature, most approaches employ some form of change detection. Therefore, these algorithms highly depend on appropriate pre-flood baselines or no-flood references. Careful selection of such images is a crucial – often manual – task in algorithms using single pre-flood images (Alexandre et al. 2020; Ulloa, Chiang, and Yun 2020). These selection procedures are challenging for systematic flood mapping operations. As such, the automated selection of these no-flood references from time series stacks has attracted attention in the literature (Hostache, Matgen, and Wagner 2012; Li et al. 2018; Zhao, Pelich, Hostache, Matgen, Wagner, et al. 2021).

Instead of selection algorithms, which often face problems in Near-real-time (NRT) operations, synthetic no-flood references can be produced from time-series analysis. Common methods include using mean or median values (Clement, Kilsby, and Moore 2018; DeVries et al. 2020Nagai, Abe, and Ohki 2021), or employing harmonic models with seasonally adjusted day-of-year estimates (Schlaffer et al. 2015). These synthetic references have the advantage of speckle suppression (Tupas et al. 2023b) and ease of automation. However, while having an essential impact on mapping performance, model selection and parameterization of these underlying models (e.g. the period length of time-series analysis) are difficult to generalize in the context of global application.

SAR change detection algorithms, where these no-flood references are used, may involve differencing or index-based methods (Schlaffer et al. 2015), time-series anomaly detection, to no-flood probability functions in Bayesian methods (Schlaffer et al. 2017). An example of the latter is the flood mapping algorithm developed at Technische Universität Wien (TU Wien), which employs a pixel-based Bayesian decision between flooded references from historical samples versus a non-food reference based on a predefined harmonic model (Bauer-Marschallinger et al. 2022). The algorithm is currently deployed in an operational setup under the Copernicus' Global Flood Monitoring service (Salamon et al. 2021). It has performed well in areas with well-defined seasonality but shows higher uncertainties for areas with ill-fitting temporal patterns, leading to overestimation.

Time-series derived estimates deviating from the actual SAR measurements can result from non-conformity with predefined parametric functions, leading to the proposal of non-parametric approaches (Colacicco et al. 2024; Refice et al. 2022). Balancing algorithm robustness and computational complexity is crucial. Rolling filters may provide an alternative. One such filter – the exponential filter – weighted filter, has been effectively used for improving soil moisture monitoring (Wagner, Lemoine, and Rott 1999). Unlike other filters, it features a near-real-time iterative formulation (Albergel et al. 2008; Bauer-Marschallinger et al. 2018) that makes it enticing for systematic mapping operations. Here, we test its use for improving flood mapping for the first time.

Most flood algorithms are tuned and tested for specific events, while mapping performance on non-flooded scenes is often ignored. This optimization of algorithms for flood scenes may disregard possible overestimation and false flagging of images as flooded where there is none. In this contribution, we present a novel time-series flood mapping assessment approach to the TU Wien algorithm to compare time-series derived no-flood references. We analyze and compare the original harmonic model with a proposed exponential-filter model. In seven study sites, we assess both non-flooded and flooded scenarios. First, we assess the no-flood models' backscatter estimates against the actual SAR image time series for 2023. Then, we analyze the false positive rate of the corresponding flood maps generated. Qualitative and quantitative analyses of flood maps are conducted using rapid mapping activations from Copernicus Emergency Management Services (CEMS) and Sentinel Asia as references.

2. TU Wien flood mapping algorithm

We present the TU Wien flood mapping algorithm's theoretical foundation and the no-flood references we intend to examine.

A Bayesian classifier, the TU Wien algorithm uses a pixel-based rule in labeling floods dependent on the posterior probability $p(F|\sigma^0)$ surpassing a predefined threshold (e.g. 50%). The posterior probability from Bayes' inference from different authors (e.g.(Bauer-Marschallinger et al. 2022; Giustarini et al. 2016; Refice et al. 2014; Schlaffer et al. 2017; Westerhoff et al. 2013)) is computed using Equation 1:

$$p(F|\sigma^0) = \frac{p(\sigma^0|F)p(F)}{p(\sigma^0|F)p(F) + p(\sigma^0|N)p(N)} \qquad (1)$$

where the conditional probability, $p(\sigma^0|N)$, to be non-flooded, is computed using the pixel's incoming backscatter against a probability distribution defined by the expected no-flood backscatter value and its temporal standard deviation (defined by the no-flood references presented in section 2.1 and 2.2). $p(\sigma^0|F)$ for the flooded case is computed against the incidence angle-dependent water distribution derived from historical samples. Lastly, $p(F)$ and $p(N)$ are the prior probabilities of a pixel being flooded and non-flooded, respectively. Non-informed priors (Giustarini et al. 2016) were used for both.

2.1. Harmonic model

The current approach of the TU Wien algorithm defines the no-flood backscatter probability distribution using the harmonic model. This model (shown in eq. 2) provides a practical way to estimate backscatter using the sum of harmonic (sinusoidal) terms to characterize its behavior over time. The presented algorithm builds upon the formulation of Schlaffer et al. (2015), where the trend is neglected and applies three iterations of harmonic terms, i.e. $k = 3$. With this realization, the model fluctuates in the order of months. Therefore, short-term backscatter variations, such as those caused by flooding, are smoothed, making it a notable no-flood reference.

$$\hat{\sigma}^0(t_n) = \overline{\sigma^0} + \sum_{i=1}^{k}\left\{ c_i \cos\frac{2\pi i t_n}{365} + s_i \sin\frac{2\pi i t_n}{365}\right\} \qquad (2)$$

Here, $\hat{\sigma}^0$ is the expected Sentinel-1 backscatter at day-of-year (DOY) t_n and is estimated based on c_i and s_i representing the harmonic parameters. The first cosine coefficient is $\overline{\sigma^0}$, equivalent to the mean Sentinel-1 backscatter for the time series.

The harmonic parameters used for this model were precalculated using a linear least squares estimation (Tupas et al. 2022) using an input time series of three years. These are the same parameters currently used for Global Flood Monitoring (GFM) operations. This three-year formulation performs overall better than the original two-year parameters (Matgen et al. 2022).

The computational complexity of the harmonic model does not allow regular updating and is best precomputed to meet operational demands (Tupas et al.

2022). This limitation leads to issues for areas with abrupt land cover change or areas deviating from the modeled seasonal trend. The latter is typically observed in bare soil, grasslands, and agricultural areas, which are more prone to backscatter fluctuations induced by vegetation and soil moisture dynamics (Vreugdenhil et al. 2018). This leads to no-flood probability distributions inaccurately reflecting the actual vegetation and soil moisture states that can lean toward flood labeling resulting in overestimation (Bauer-Marschallinger et al. 2022).

2.2. Exponential filter model

To compensate for such overestimation, we seek alternative methods that could be updated dynamically, allowing a more accurate and up-to-date representation of vegetation or soil moisture dynamics. Consequently, we considered shorter moving averages or rolling filters. One such filter applies exponential weights decaying through time. We present the continuous formulation of the exponential filter model in equation 3 taken from Wagner, Lemoine, and Rott (1999) but adopted to estimate backscatter, $\hat{\sigma}^0$, at some day in time: t_n.

$$\hat{\sigma}^0(t_n) = \frac{\sum_i^n \sigma^0(t_i)e^{-\frac{t_n-t_i}{T}}}{\sum_i^n e^{-\frac{t_n-t_i}{T}}} \qquad (3)$$

where $\sigma^0(t_i)$ is the observed Sentinel-1 backscatter at time t_i. T is the equations' characteristic time length parameter, representing the timescale of backscatter variation in days.

Preliminary tests with other rolling filters (like mean and median) showed similar or slightly worse performance than exponential filters and is presented in the Supplementary material (Section D) for brevity. Nonetheless, the practical prospect of the exponential filter lies in its recursive formulation (Bauer-Marschallinger et al. 2018). While mathematically giving the same result, the recursive formulation allows updated estimates to be calculated at new time steps with only incrementally updated gain value and new measurements, dramatically reducing computational requirements compared other rolling filters where a recursive formulation is not feasible. However, to better illustrate the effect of T parameter and our current focus on performance rather than efficiency, we only present the continuous form in this work.

To reduce the volume of datasets used in the continuous formulation, we excluded measurements with effective weights of less than 0.05. This procedure roughly corresponds to considering measurements within the time range of $[t_n - 3T, t_n)$ (excluding t_n).

In soil moisture studies, the selection of T value is topic of ongoing investigation (Albergel et al. 2008; Pellarin, Calvet, and Wagner 2006), where Paulik et al. (2014) established basic relations of T values to soil depth from correlation analysis against in-situ reference measurements. As the optimal value of T in flood mapping is still unknown, we aim to determine a suitable T parameter for robust flood mapping by experimenting with different values. We test multiple T, i.e. $T = 10, 20, 30, 40, 60, 90$, and 120.

From preliminary tests, we found that exponential filter estimates with shorter time-series inputs do not suppress speckle well. Therefore, input radar backscatter images for exponential filter were despeckled using Lee-Sigma Filter (Lee 1983; Lee et al. 2009) with 3×3 kernel size.

2.3. Standard deviation

To form the no-flood backscatter probability distribution, we assume its form as Gaussian based on suggestions from the literature (Refice et al. 2014; Schlaffer et al. 2017; Sherpa et al. 2020). Thus, in addition to an expectation value, a degree of dispersion (standard deviation) is required.

We compute the standard deviation using Equation 4 based on Bauer-Marschallinger et al. (2022) approach, given by the square root of the time-independent sum of squared errors, $SSE(\sigma^0)$, between the actual backscatter time-series and the estimated values from the time-series models, divided by the models' degrees of freedom v.

$$std = \sqrt{\frac{SSE(\sigma^0)}{v}}[dB] \quad (4)$$

Here v is the degrees of freedom and is solved by $n - (2k + 1)$ for the harmonic model and $n - 2$ for the exponential filter model, where n is the number of observations. For the harmonic model, the standard deviations were computed from the same three-year period used to estimate the parameters. In contrast, the exponential filter standard deviations, regardless of T values, were computed using the 2023 time series.

2.4. No-sensitivity masking and post-processing

After initial labeling, the TU Wien algorithm applies a no-sensitivity masking procedure that tags pixels where the BI is not feasible. This includes areas with 1) extreme local incidence angle where the flood probability model is invalid, 2) conflicting flood and no-flood probability distributions, and 3) measurement outliers. We refer the reader to Bauer-Marschallinger et al. (2022) for further details on no-sensitivity masking. This study uses the same no-sensitivity mask thresholds as the original algorithm.

Finally, we omit the majority filter-based post-processing step, as we found that it results in undesired over- and under-labeling. Further exclusion masking (Zhao, Pelich, Hostache, Matgen, Cao, et al. 2021) were not applied to allow for comparisons and observe possible improvements in these areas.

3. Materials and study sites

To give an overview of the materials and methods used in this study, Figure 1 shows the different phases of analysis. The green panel explains derivation from the Sentinel-1 data cube (section 3.1) of the TU Wien algorithm and the no-flood reference models, we described in described in section 2. To ensure a globally applicable analysis, we endeavor to analyze as many sites as possible. The purple panel represents the site selection process discussed in section 3.4. We further ensure robustness in no-flood scenarios by extending our analysis to understand temporal behaviors. The yellow panel shows the no-flood time series analysis found in Section 4.1. Finally, we conduct traditional comparisons for a reference flood event for each test site. The orange panel represents the flood mapping accuracy assessment described in section 4.2.

3.1. Sentinel-1 data cube

To produce the flood maps and their corresponding no-flood reference images analyzed in this study we use the VV polarized subset of Sentinel-1 (Torres et al. 2012) data cube maintained by TU Wien and EODC (Wagner et al. 2021). The data cube comprises curated Sentinel-1 Ground Range Detected (GRD) image tiles with $20\,m \times 20\,m$ pixel size and organized using the T3 tiling level (300 km x 300 km extents) of the Equi7Grid system (Bauer-Marschallinger, Sabel, and
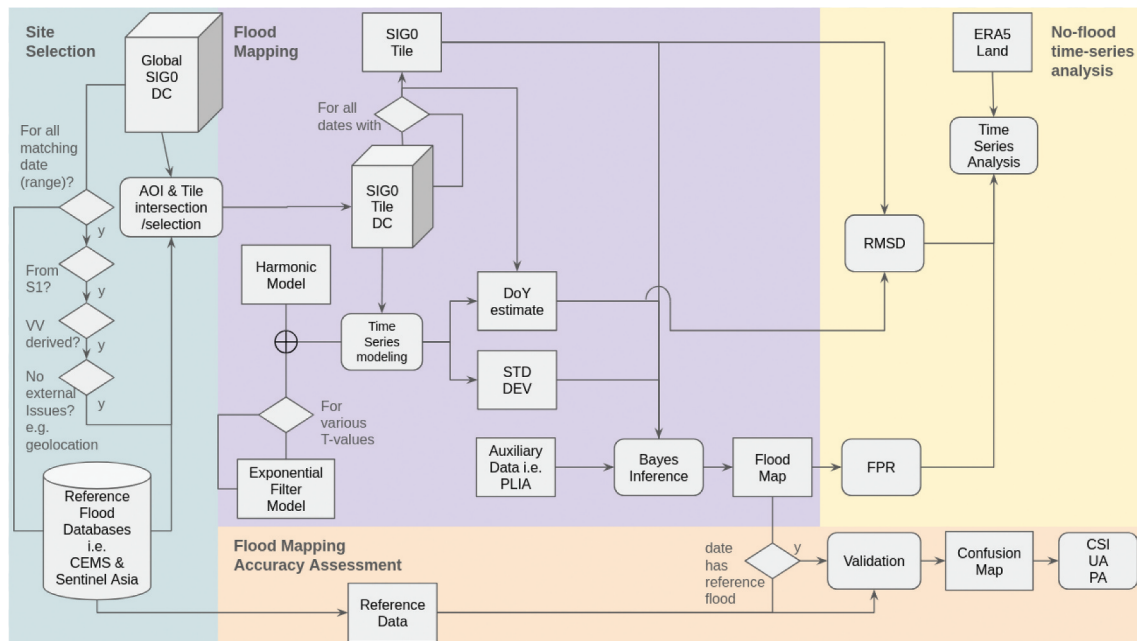
Figure 1. Methodological flowchart and phases of analysis. Green panel: site selection procedure. Purple panel: flood mapping algorithm. Yellow panel: No-flood time-series analysis. Orange panel: flood mapping accuracy assessment.

Wagner 2014). Spatial analysis performed throughout this study were conducted in the same tiling and grid system using the python based Yeoda software stack https://github.com/TUW-GEO/yeodahttps://github.com/TUW-GEO/yeoda (accessed 20 July 2024).

3.2. Ancillary data

To understand the environmental conditions and spatiotemporal backscatter dynamics governing our flood mapping results, we cross-referenced several ancillary datasets that were re-gridded and reprojected to the Equi7Grid tiles.

Soil temperature and water content are crucial factors in explaining overestimation (Lin et al. 2019), and were used to rule out floods in images in which frozen and dry soils cause large swaths of low backscatter. ERA5-Land (Muñoz-Sabater et al. 2021) Daily Aggregated data accessed from Google Earth Engine (Gorelick et al. 2017) were used to calculate the means of soil temperature and volumetric soil water at the topmost level (0 – cm).

Furthermore, we used the ESA WorldCover (2021) (Zanaga et al. 2021) to explain spatial patterns. And, where available, Crop Map (2022) (d'Andrimont et al. 2021) for finer separation of crop types. Land cover

and crop type (and their associated cropping practices) give further insights into the flood maps and overestimation patterns.

3.3. Reference Flood and Water Maps

We use activation-based flood maps as a reference for accuracy assessments under the premise that operational service relies on expert intervention in (semi-automated) map generation and quality assurance. These maps are reasonable alternatives in lieu of actual ground truth flood data.

In this regard, Copernicus Emergency Management Services (CEMS) (Joubert-Boitat, Wania, and Dalmasso 2020) rapid mapping vector flood extents and associated ancillary data (e.g. AOI, Hydrology) were retrieved from https://emergency.copernicus.eu/((accessed on 13 March 2024). Sentinel Asia (Kaku 2019) vector flood extents were also downloaded from https://sentinel-asia.org/EO/EmergencyObservation.html (accessed on 13 March 2024). The reference flood maps were rasterized and reprojected to the Equi7Grid tiles.

To differentiate semi-permanent and permanent water bodies from flood results (Wieland and Martinis 2019), we use the CEMS hydrology dataset for the assessed flooded AOIs. For comparisons of entire tiles

and where CEMS data is absent, we use Copernicus DEM (Fahrland et al. 2020) Water Body mask. Both datasets are used to mask out water areas for both qualitative and quantitative assessments.

3.4. Study sites

All flood mapping activations listed in the CEMS and Sentinel Asia databases from March 2023 to November 2023 were considered in our study. The aim is to analyze a diverse representation of environmental and climatic conditions, allowing for global generalization. However, emergency response maps as reference data require careful inspection, selection, and contextualization to obtain nuanced assessments. Thus, we implement a rigorous matching and screening procedure.

A preliminary search of the two flood mapping services' activations was screened for flood maps delineated using Sentinel-1. This was done to ensure that our experimental results and the reference match temporally and spatially. The reference flood maps and corresponding Sentinel-1 images were scrutinized to ensure that there were no obvious geolocation errors and that flood extents could be reasonably determined from VV polarized data – for which the algorithm is tuned for. In cases with more than one area of interest (AOI), we selected the AOI with the most prominent flood coverage. The final area of

interest for flooded assessments is selected based on the intersection of the Equi7Grid tile that contains the most significant portion of the AOIs. In contrast, the whole data cube tiles are used for non-flooded assessments.

Four test sites covered by CEMS are situated in Europe, where there is a noted increase in flood anomalies (Tarasova et al. 2023). The flooding incidents in Scotland (Graham et al. 2023), Slovenia (Bezak et al. 2023) and Greece were triggered by extreme precipitation, the latter noted for its exceptional rainfall duration and intensity (Dimitriou et al. 2024; He et al. 2023). Meanwhile, CEMS reports that the snow melt contributed to the flood event in Latvia. The Sentinel Asia activations describe the events in Vietnam and India as caused by heavy rainfall, while tropical cyclone Doksuri caused the Philippine mapped event. The area was subjected to intense rainfall from a preceding tropical depression (He et al. 2023).

When plotted against global environmental stratification data (Metzger 2018), shown in Figure 2, one can see that our test sites contain a good mix of climate types and different seasonality inclinations. Metadata summary on the seven study sites is found in Table 1; these include the reference flood activation information, and the dominant Global environmental stratification (GEnS) zones per tile.
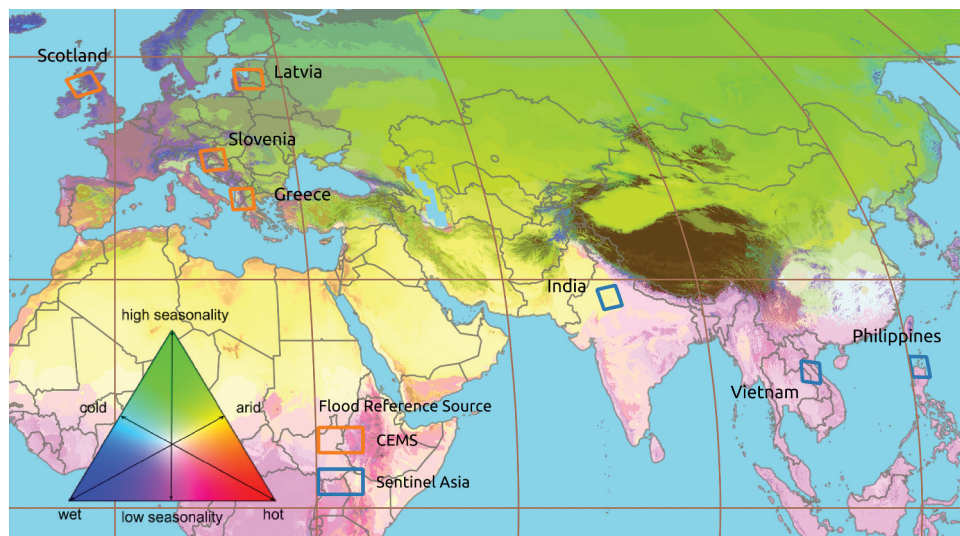

Figure 2. Location of study sites (Equi7Grid tiles) colored based on available reference flood maps overlain on global environmental stratification (GEnS) layer (Metzger 2018).

Table 1. Study sites and metadata on Equi7grid tile details, reference flood maps and climate zones.

Location	Rel. Orbit	Source	Activation Code	AOI/Subset	Est. Area (km^2)	Date	GEnS zone[a]
Scotland	A030	CEMS	EMSR698	03	20	2023.10.08	E, J
Vietnam	D091	Sentinel Asia	FL-2023-000179-VNM	Nghe An & Ha Tinh	286	2023.09.30	M, R
Greece	A102	CEMS	EMSR692	01	730	2023.09.07	K, L
Slovenia	A146	CEMS	EMSR680	04	3	2023.08.05	G, J
Philippines	D032	Sentinel Asia	TC-2023-000121-PHL	–	416	2023.07.28	R
India	A027	Sentinel Asia	FL-2023-000112-IND	–	537	2023.07.16	M, P
Latvia	D080	CEMS	EMSR657	01	55	2023.04.03	G

[a]Global environmental stratification (GEnS) zones: E-cold and wet, G-cold and mesic, J-cool temperate and moist, K-warm temperate and mesic, L-warm temperate and xeric, M-hot and mesic, P extremely hot and arid, R extremely hot and moist.

4. Assessment methodology

4.1. Reference image and No-flood time-series assessment

To compare the performance of the no-flood time series backscatter models (and T parameterization), we compute the root-mean-square deviation (RMSD) (Barsi Kugler et al. 2018) between the estimates and actual Sentinel-1 measurements per image acquisition date for 2023. RMSD is computed using Equation 5:

$$RMSD(t_n) = \sqrt{\frac{\sum_{i=0}^{N-1} (\sigma_i^0(t_n) - \hat{\sigma}_i^0(t_n))^2}{N}} [dB] \quad (5)$$

where $\hat{\sigma}^0(t_n)$ is the estimated Sentinel-1 backscatter per pixel for a given time tn, while $\sigma^0(t_n)$ is the observed Sentinel-1 backscatter for that pixel at the same time and N is the total number of valid pixels.

Flood maps are then produced for every Sentinel-1 acquisition date irrespective of flood occurrence. We create maps based on each no-flood reference for each date using the harmonic model and the exponential filter at varying T values.

We limit our assessments to one relative orbit per tile, which is selected to match the flooded reference maps' source Sentinel-1 image's relative orbit. At a specified relative orbit, with a 12-day revisit time, there are about 30 acquisition days per study site for a year. This mapping during each satellite pass simulates the automated procedure performed in the flood monitoring operations. Up to 240 flood maps for 2023 were created for each study site. We note actual flooded acquisition dates for each tile based on documented reports and flood mapping service activations, while all other acquisitions are assumed to be entirely non-flooded.

$$FPR = \frac{FP}{FP + TN} \quad (6)$$

After masking permanent and seasonal water, we can compute the false positive rate (FPR) using equation 6 based on the assumption that all remaining flooded pixels are false positives (FP) and non-flooded as true negatives (TN) (Barsi Kugler et al. 2018; Tupas et al. 2023a). The FPR and RMSD are temporally plotted and cross-referenced with ERA5-Land data for soil temperature and volumetric soil water for the uppermost soil layer. We do this to explore possible overestimation through time and attribute its possible causes vis-à-vis the no-flood model used for flood mapping. To confirm the difference in performance of the tested no-flood models, we perform pairwise comparisons between all models. For each two no-flood model comparison, we employ paired statistical tests between the aggregated FPR differences from all study sites.

4.2. Flood map assessment

In addition to the no-flood evaluations, we analyze the performance of our algorithm on dates where reference flood maps are present, described in Table 1. Before quantitative assessments, we harmonize our generated flood map with the reference data. First, the maps are clipped to reference data AOIs. These are provided as a separate vector layer for CEMS results, while the bounding box of the Sentinel Asia vector results is used as AOIs. Then, we apply the corresponding water masks before creating confusion maps and tables.

Subsequently, we compute accuracy assessment metrics for all flood maps. The metrics, Critical Success Index (CSI), User's Accuracy (UA), and Producer's Accuracy (PA), shown in equations 7, 8, and 9:

$$CSI = \frac{TP}{(TP + FP + FN)} \qquad (7)$$

$$UA = \frac{TP}{(TP + FP)} \qquad (8)$$

$$PA = \frac{TP}{(TP + FN)} \qquad (9)$$

where TP is the true positive, TN is the true negative, FP is the false positive, and FN is the false negative counts derived from the binary confusion matrix. These metrics are chosen to express the flooded maps' overall performance via the CSI (Landuyt et al. 2019), while over- and underestimations from UA and PA (Barsi Kugler et al. 2018). To compute these accuracy assessment metrics for the flood maps against the vector reference data, we use ABCRaster https://github.com/TUW-GEO/ABCRasterhttps://github.com/TUW-GEO/ABCRaster (accessed 20 June 2024) to automate the procedure. Relying solely on a few metrics

may not fully capture mapping performance. Therefore, we conduct a qualitative visual evaluation of the confusion maps.

5. Results

5.1. No-flood time series

The plotted RMSD and FPR against ERA5-Land surface soil temperature and moisture shown in Figures 3, 4 and 5, are sample plots for the Latvia, Greece, and India study sites, respectively. We include the time-series plots for the rest of the sites in the Supplementary material for conciseness.

The figures present three horizontal panels depicting the performance of the no-flood references using the harmonic and exponential filter models at various T values and soil properties per Sentinel-1 acquisition per tile in a specific relative orbit. The top panel shows the FPRs per flood map for every Sentinel-1 acquisition date for the tile, assuming there is no actual
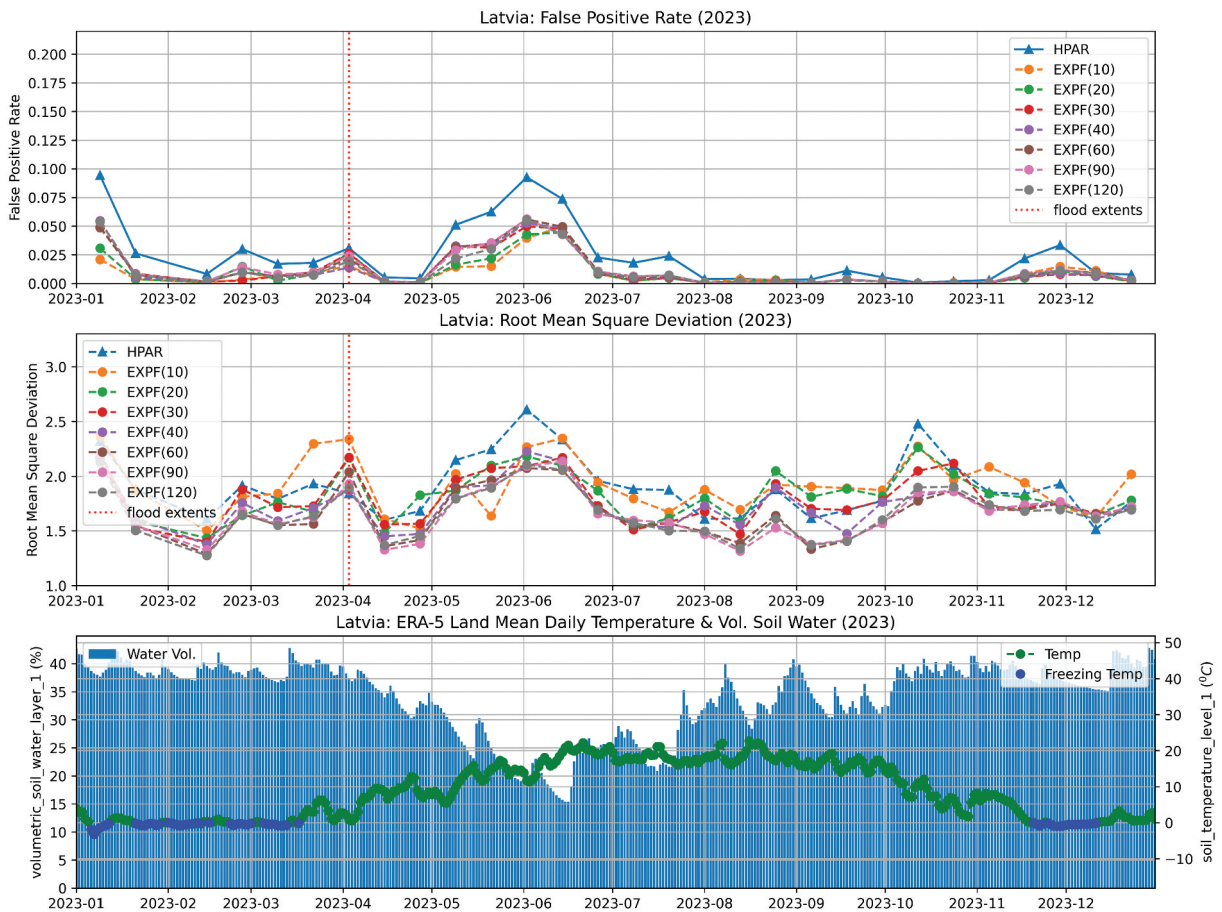

Figure 3. Temporal plots of false positive rate, root mean square deviation, and ERA5-land soil temperature and volumetric soil water for the Latvia study site.
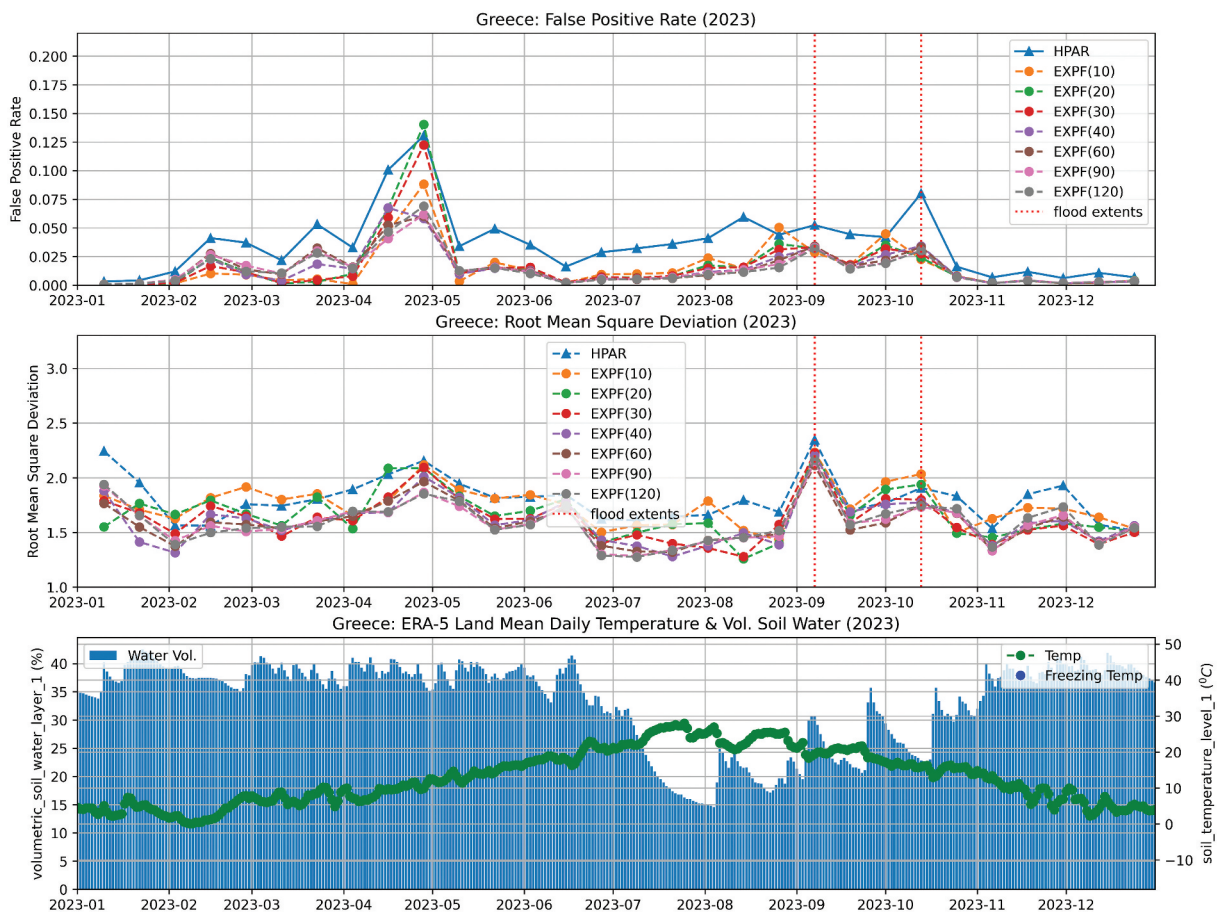
Figure 4. Temporal plots of false positive rate, root mean square deviation, and ERA5-land soil temperature and volumetric soil water for the Greece study site.

flood. The middle panel shows the RMSDs for no-flood reference estimates versus the actual Sentinel-1 data. The bottom panel shows the ERA5-Land temperature and volumetric water content at the top-most soil layer (0–7 cm).

5.1.1. Latvia

We present the result for the Latvia test site (Figure 3) as a representative study site with a cool temperate climate. Similar phenomena can be observed with the Slovenia and Scotland study sites (in the Supplementary material).

Regarding FPRs, we observed peaks at the beginning and end of the year corresponding to frozen soils at those specific dates. As frozen soils exhibit a similar significant drop in backscatter (Baghdadi et al. 2018) thus is easily mistaken as floods. A smaller peak in FPR was observed during the flooding event in April.

A prolonged peak is observed toward the summer months, corresponding to relatively dry soils from the ERA5-Land data. This rise in false positives relates to lower backscatter signals of drier soils being mistaken for the low backscatter caused by specular reflection of inundated areas as radar backscatter increases with soil moisture content (Ulaby, Bradley, and Dobson 1979) except for arid environments where subsurface scatterers are present (Wagner et al. 2024). The scattering behavior of wet soil changes fundamentally once standing water forms at the surface. The peaks in RMSD mostly correspond to the same peaks in FPR. However, it was observed that there is a more prominent peak in RMSD compared to FPR during the documented flood, which is the expected behavior for a no-flood reference.

For both the FPR and the RMSD, the HPAR performs less well than the exponential filter. In terms
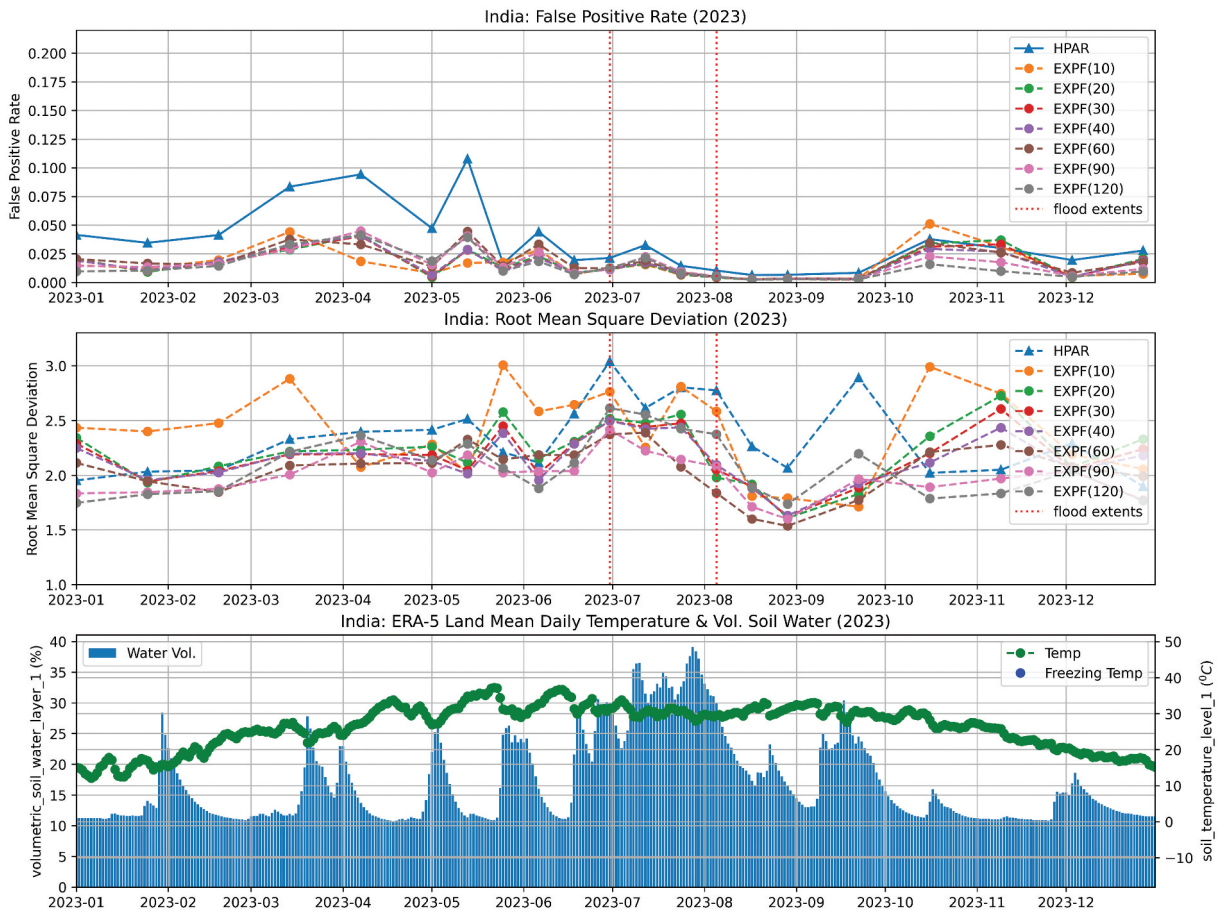
Figure 5. Temporal plots of false positive rate, root mean square deviation, and ERA5-land soil temperature and volumetric soil water for the India study site.

of exponential filter T value, most perform similarly. Aside from $T = 10$ and $T = 20$, they have varied performances relative to the other T values, sometimes getting the best and worst results in others.

5.1.2. Greece

Greece (Figure 4) is presented to show the behavior of a warm temperate study site. Regarding the FPR, it is observed that the exponential filter model performs better than the harmonic model for most of the year. Like the previous plots, the lower T values showed inconsistent performance compared to the other T values. The performance of other T values is difficult to differentiate. A similar pattern is observed for the RMSD, where the harmonic model consistently shows higher values than the exponential filter model.

A significant flooding event on this tile lasted from most of September to early October (He et al. 2023). We

observed elevated RMSD and FPR values during this period.

In contrast, there is a significant increase in FPR from most of April to May, which does not have a distinct rise in RMSD. Looking at the ERA5-Land plots, this April-May increase does not correspond to frozen soils or dry conditions. Thus, the most likely cause is the start of agricultural activity in the region, where bare ground or emergent vegetation typically exhibits low backscatter (Harfenmeister, Spengler, and Weltzien 2019) and is maybe mistaken for flooding.

The considerable spike in FPR here can be explained by the large proportion of the agricultural area in the tile and the particular crops grown in this area. The more significant difference in performance between the harmonic model and exponential filter can be attributed to the same issue and is explained further in the spatial context in section 5.2.
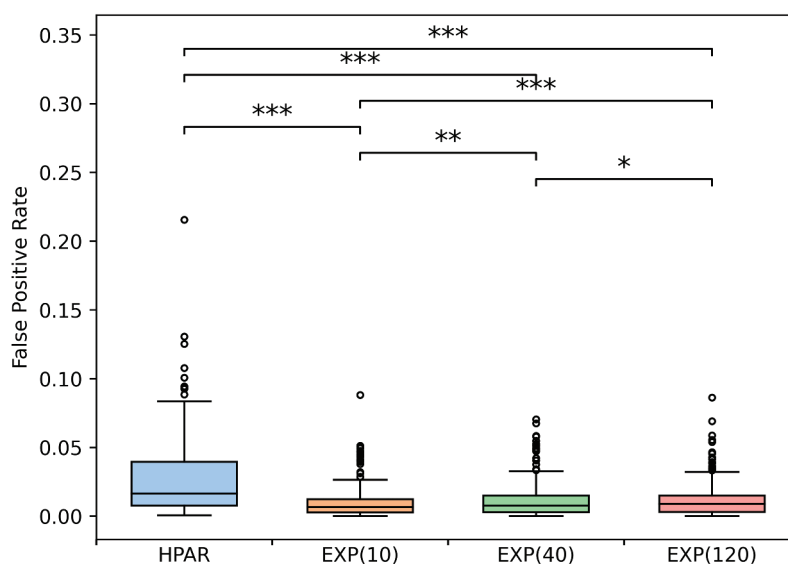
Figure 6. Box and whisker plots of the aggregated false positive rates with the significance level. ***: p-values < 0.001, **: p-values < 0.01, *: p-values < 0.05, and ns: p-values > = 0.05.

5.1.3. India

The Indian study site (Figure 5) is in an arid climate. Therefore, dry soil conditions primarily drive the temporal dynamics of FPR and RMSD. An increase in FPR and RMSD is observed from April to May due to dry soil conditions. A larger increase in RMSD was observed during the prolonged flood event in July. Compared to dry conditions, no prominent increase in FPR was observed. For the India study site, the harmonic model and all T parameterizations of the exponential filter performed similarly for the second of the year, with a noticeable difference from the start of the year until June.

5.1.4. Southeast Asia

The Vietnam and Philippines test sites have tropical climates and show less variation in the FPR and RMSD. This observation can be attributed to relatively stable soil moisture and temperature throughout the year.

In the case of the Philippines (Figure A1), a large percentage of the tile are dense tropical forests; thus, backscatter variations are small (Zhao, Pelich, Hostache, Matgen, Cao, et al., 2021), leading to stable tile-based aggregates where no peaks were observed in RMSD and FPR. The harmonic model and the exponential filter (regardless of the value T) are almost indistinguishable.

For Vietnam (Figure A3), there is greater variance in terms of RMSD as the climate is not purely hot and humid for the whole tile. Like Indian example, the

harmonic model also performs worse than the exponential filter for the year's first half. Unlike the other test sites, the harmonic model and exponential filter perform similarly for no-flood scenarios in the Southeast Asian test sites.

5.1.5. General perspective on false positive rates

To get a generalized perspective on the no-flood models' FPR performance, we further analyze the aggregated observations from all study sites. As observed in the time series metrics plots, the no-flood models' FPR performance show obvious similar trends following known environmental drivers. Thus, to differentiate the models, we statistically test the significance of the FPR differences per pair of no-flood models from all test sites.

The paired FPR differences between the various no-flood models showed significantly skewed (non-normal) distributions. Hence, the non-parametric Wilcoxon test (Pratt 1959; Wilcoxon 1945) was used instead of the paired t-test to test for significance. For this test, the null hypothesis (H0) states that there is no significant difference between the compared no-flood models. While the alternative hypothesis (H1) indicates a significant difference.

Figure 6 shows box and whisker plots of the aggregated False Positive Rates of selected no-flood reference model. Shown on top is the significance based on the pairwise Wilcoxon test. Almost all no-flood models showed significant statistical difference compared to

others, except for T = 60 compared to T = 90 and T = 120 (see Table B1). Notably, the HPAR model against all Exponential model showed the highest (***) significance, while between the exponential filter models per T values show lower significance as T values become larger. On the box plots, we can see median FPR values of each no-flood model. The harmonic model in general shows about 0.027 FPR to less than 0.013 for all exponential filter models. Meanwhile, the differences in median FPR values between the exponential filter model at various T values are very small (although statistically different).

5.2. False positive frequency mappings

To delve deeper into the issue of overestimation, we shift our focus from analyzing the time series data at the tile level to considering the spatial dimension. By generating flood frequency maps (Pelich et al. 2017) and excluding instances from flood dates, we can represent the occurrence of false positives in each pixel. These maps enable us to assess how the false positive rates align with land cover and crop type. We compare the false positive (FP) frequency map based on the harmonic model and the exponential filter with T = 40 alongside the EU Crop map for specific locations as examples.

Consistent with the initial findings of Bauer-Marschallinger et al. (2022), we find further evidence of overestimation due to agriculture. In the Greek study site, as shown in the upper row of Figure 7, there is a noticeable variation in false positive frequency at the level of individual agricultural plots. Many agricultural plots are falsely labeled as flooded up to one-third of the year, some even exceeding 40%, and thus indicating a clear disadvantage of the harmonic modeling at this location.

There are noticeable differences in FP count between plots growing maize and cereals compared to industrial crop plots, the latter being more easily misinterpreted as flood labels. K. He et al. (2023) identify cotton as the most prevalent industrial crop. The sensitivity of cotton fields to false labeling can be attributed to agricultural practices (e.g. field flooding) and the higher backscatter of the cotton plant in the middle of the cropping stages, leading to a higher temporal model variance (Maity et al. 2004).

The grasslands of the Slovenian test site shown in the lower row of Figure 7 have higher FP frequencies.

From open optical satellite imagery, these areas appeared to be seasonally flooded and were missed by water masks. In these regions, the exponential filter shows fewer FPs. In the northeast corner of the map, some distinct agricultural plots are also apparent in the frequency maps, such as rape. Maize has fewer FPs on this site compared to Greece.

Bare soils, grasslands, and croplands show more FPs than other land cover types. In terms of other specific crops, we observed with elevated FPs from other test sites include wheat, cereals, and rice (see Section C). These crops have been shown to have low backscatter periods during their growing stages Chang et al. (2021); Harfenmeister, Spengler, and Weltzien (2019); Vreugdenhil et al. (2018). However, there seems to be a site variation in the FP frequency of most crops.

In both exemplar flood frequency maps, the spatial patterns of FP are similar. However, the harmonic model shows significantly more FPs than the exponential filter, consistent with the temporal FPR plots.

5.3. Flood scenarios quantitative analysis

Next, we focused on flood mapping performance on flooded dates with reference flood maps. The critical success index of the flood maps using the baseline harmonic no-flood reference where 60.87%, 44.02%, 56.38%, 41.90%, 58.08%, 68.04%, and 54.71% for the study sites in Latvia, India, the Philippines, Slovenia, Greece, Vietnam, and Scotland respectively. On average, the seven study sites got 67.12% for User's Accuracy and 79.53% for Producer's Accuracy. These accuracy assessment results are consistent, but are nominally lower, with the similarly sized events and same environmental conditions examined when using the TU Wien flood mapping algorithm (Tupas et al. 2023a). This study obtained lower values because of non-application of external exclusion masks.

To differentiate the performance of harmonic model versus the exponential filter, we show Figure 8 where we plot the differences in CSI, UA, and PA of all our test sites.

Regarding CSI, we compare the performance of the no-flood references within sites. The varying sizes of flood extents, as shown in Table 1, influence the CSI (Stephens, Schumann, and Bates 2014). Consequently, we avoid direct inter-site comparisons
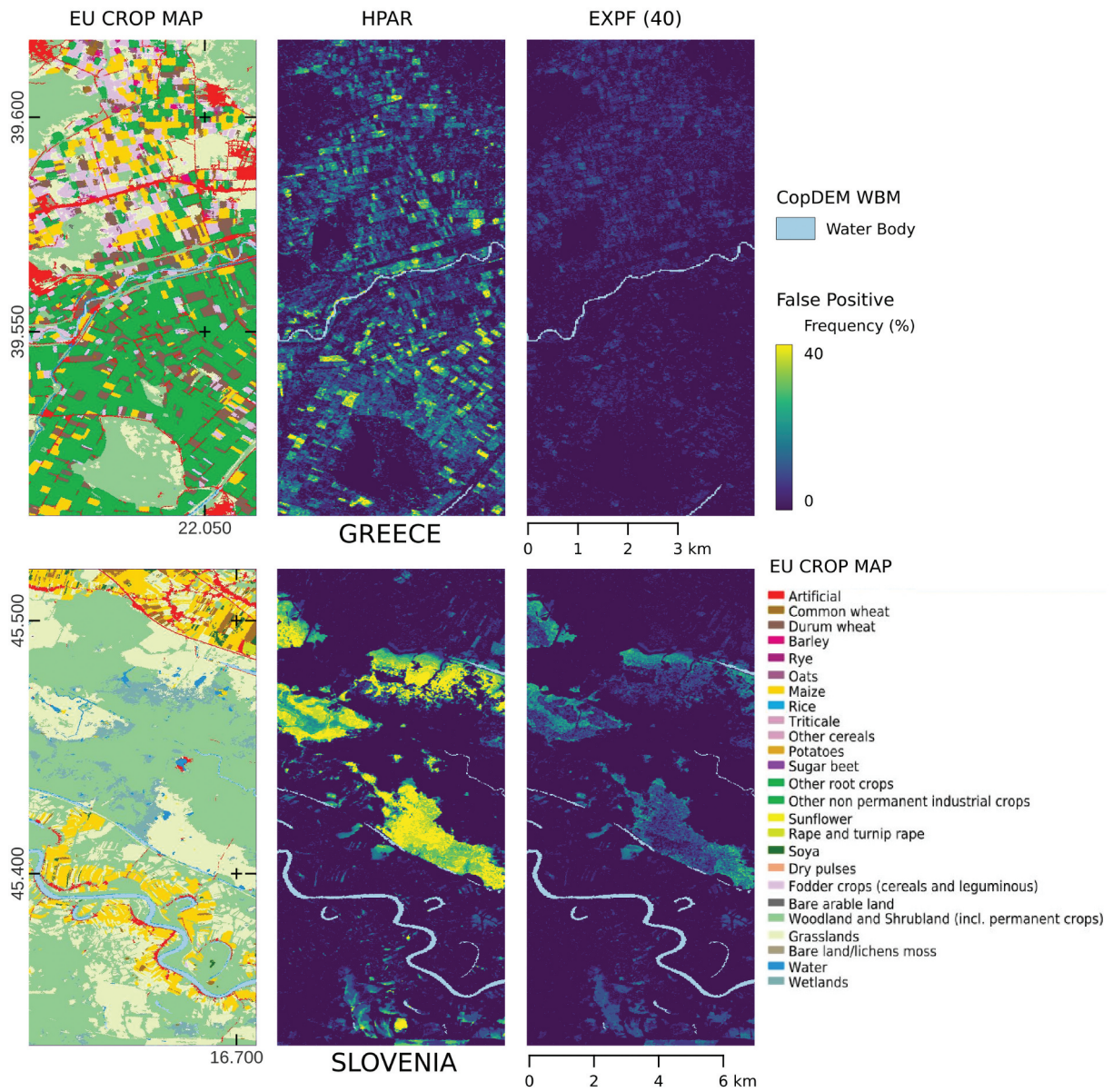
Figure 7. Flood false positive (FP) frequency maps of Greece and Slovenia study sites. Greece *N*=26, Slovenia *N*=29 where N is number of observations less actual flooded images. EU crop cover map is provided as reference.

Figure 8. Heat maps summarizing difference in critical success index, user's accuracy, and producer's accuracy of flood maps between the harmonic model and exponential filter models with various t parameters (y-axis) for the seven study sites (x-axis).

based on the CSI. We focus on the comparison of the no-flood models in regard to the original harmonic model method, thus we present the differences relative to the HPARs shown in Figure 8. With this differencing, we reduce the bias in CSI to be able to make more generalized observations.
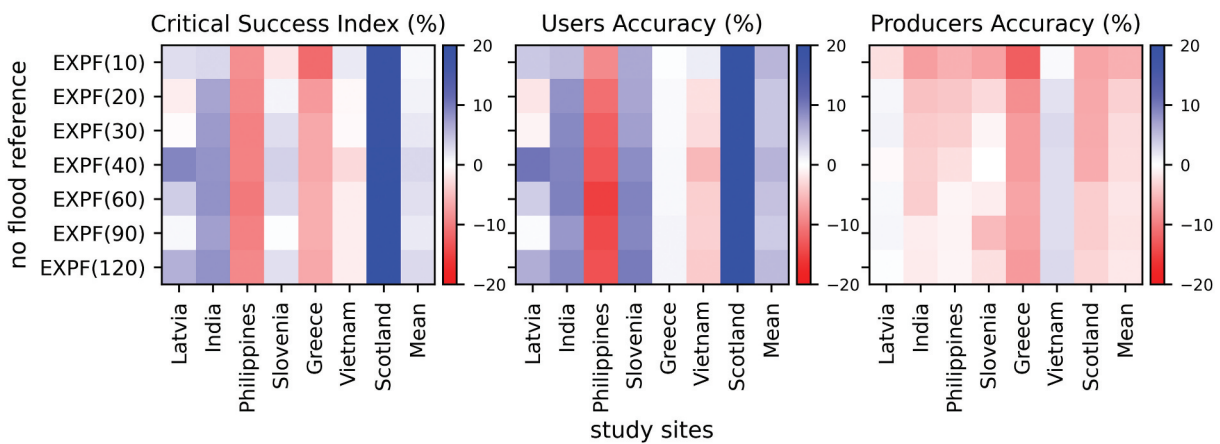
The exponential filter performs better than the harmonic model in Latvia, Slovenia, and India. In Vietnam, the harmonic model is comparable to the exponential filter. Meanwhile, the exponential filter performs significantly better at the Scotland study site. The harmonic model performs better than the exponential filter in the Greece and Philippine study sites. We further discuss the cause of the poor performance of the exponential filter in section 5.4.3 on prolonged floods that are apparent in these two test sites.

In terms of the T parameter, the CSI difference decreases as T increases for both study sites in Southeast Asia. This observation is consistent with our initial results (Tupas et al. 2023b), where the harmonic model outperforms the long-term means as a no-flood reference. Apart from the Scotland study site, which shows slightly increasing performance at larger T values, all other test sites show better performance at mid T values, most often peaking at $T = 40$. This is reflected by the mean of the differences for the tested sites also peaking at the same T, with a modest 3.06% in CSI.

The middle panel in Figure 8 shows the UA plots of all study sites. It should be recalled that the UA is inversely related to the commission error. In most study sites, aside from the Vietnam and Philippine study sites, we see that the exponential filter typically shows less overestimation. Only the Scottish case showed a stark difference in UA values, while most others showed minor improvements. On average, there was 5.75% increase in the User's accuracy at the same peak T value of 40.

Commission errors increase with increasing exponential filter T values in Scotland, Vietnam, and the Philippines. In contrast, a middle peak is observed in Latvia and India. Furthermore, we note an almost stable but slightly decreasing trend in Greece and Slovenia.

In the rightmost panel in Figure 8, we plot the PA – the inverse of omission errors, of the sites we tested. In general, the harmonic model flood maps show less underestimation. Greece is the only site with severe

underestimation in the exponential filter. Most sites show slightly fewer omission errors. The exponential filter T values show a mainly increasing PA trend. Unlike the CSI and UA, PA of the exponential filter models had a decrease compared to the harmonic model. The best performing T value in case is $T = 120$ with 1.79% mean decrease, while at $T = 40$ with 2.58% decrease on average was observed.

5.4. Flood scenarios confusion maps

To put the comparative metrics discussed into spatial context, we show exemplary confusion maps highlighting the benefits and issues with the no-flood reference models we tested.

5.4.1. T parameter of the exponential filter

We present the study site in Scotland shown in Figure 9. Here, we show the eight confusion maps pertaining to the harmonic model and the exponential filter at varying T. The harmonic model produces more false positives compared to the exponential filter.

Although the flood delineations from the exponential filter remain relatively consistent, intermediate values, such as $T = 40$ to $T = 90$, visually perform better. We observed higher and lower T values to have more No-sensitivity masked (NSM) pixels in both flooded and non-flooded areas. Similarly to most cases, this example shows more TP pixels for the harmonic model, thus higher PAs. Based on these visual observations and optimal performance indicated by the mean differences, $T = 40$ is an appropriate initial choice for the flooded scenario.

5.4.2. Reduced overestimation

For conciseness, we show the exemplary performance of the harmonic model and the exponential filter at $T = 40$ in Figure 10, as the performance based on the T values, in most cases, reflects that of the Scotland site depicted above. We show insightful subsets of the confusion maps for four other sites covering diverse environmental zones.

The confusion maps for the study site in Latvia are shown in the first row of Figure 10. This study site suffers from high commission errors and is most apparent in sparse blobs of FP pixels. There are larger FP blobs from harmonic model flood maps compared to the exponential filter maps. Some of the reduced FP patches in the exponential filter model appear on
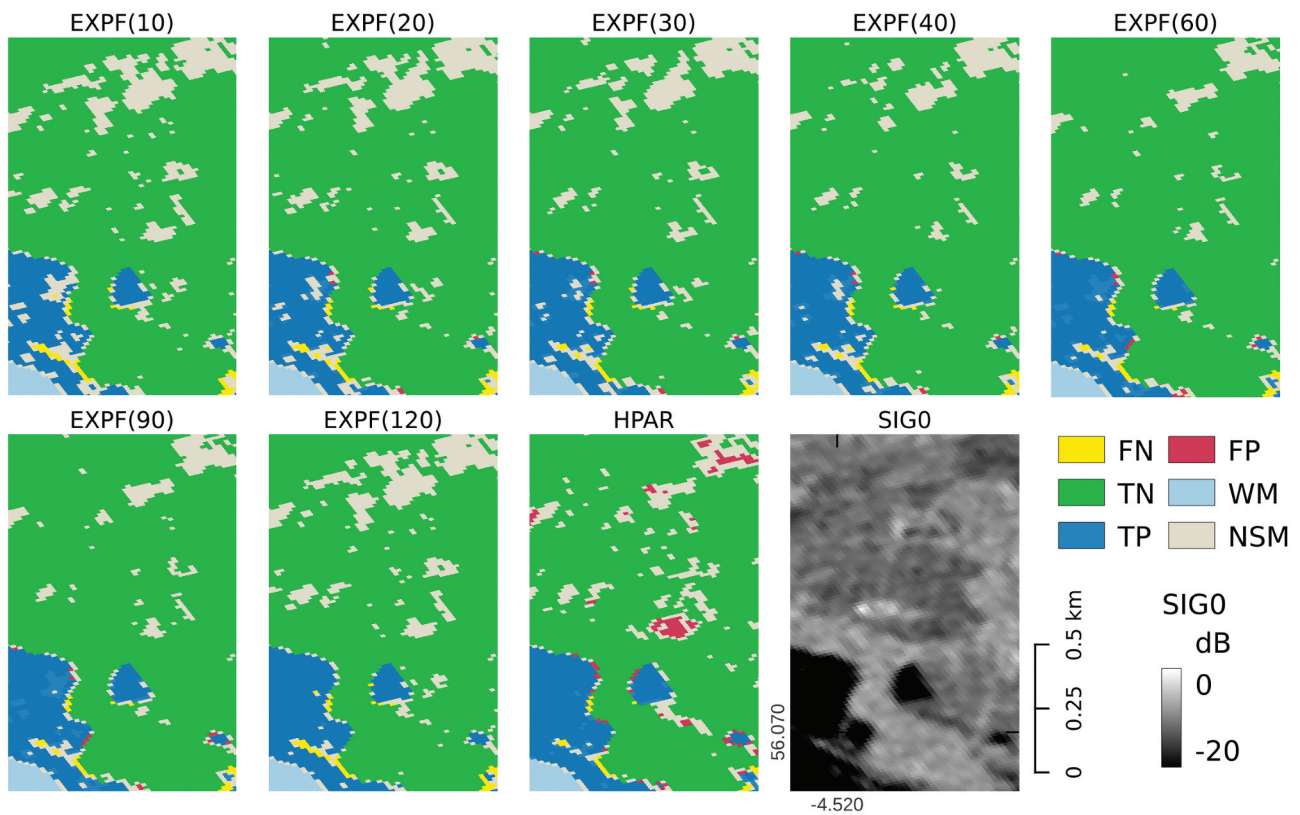
Figure 9. Scotland study site confusion maps, computed from flood maps on 2023.10.08 generated using the harmonic model (HPAR) and exponential filter (EXPF) at various *T* values against CEMS rapid mapping product. Legend: FN - false negative, TN - true negative, TP - true positive, FP -false positive, WM - reference water mask, NSM - TU Wien no sensitivity mask. Flooded SIG0 backscatter is presented as reference.

dense vegetation and might be removed through exclusion masking. This can be perceived both positively and negatively; it suggests potentially lesser dependency on exclusion masking but also indicates that there might be limited improvement if they were masked.

In contrast, the exponential filter maps have sparse no-sensitivity masked pixels within the flooded area, thus missing TP pixels. Recall that the no-sensitivity mask covers pixels with similar no-flood and flooded distributions. FNs are a minor issue for both maps tested in this study site.

The second row of Figure 10 shows the confusion maps for the Indian tile. This map shows reduced flood labels from the exponential filter for TP and FP areas. Consequently, this reduces the commission errors but increases the omission errors similar to the temperate study sites discussed above.

A subset of the Philippine test site is shown in the third row of Figure 10. A cursory check of the Philippine Rice Information System (https://prism.philrice.gov.ph). (Mabalay et al. 2022) reveals that

this area is mainly cultivated for rice. The harmonic model showed more prominent areas of omitted TP but consequently fewer FP. This area appears to be problematic for the static harmonic model to estimate. We attribute this to year-to-year variations in the rice planting season (Gutierrez et al., 2019), which causes temporal shifting leading to higher than usual variability in the temporal radar back scatter signature. While this issue occurs for most land cover types, this is very pronounced in rice fields due to paddy flooding (very low backscatter) at start of season. This results in ill fitting no-flood reference causing the significantly large no-sensitivity masked area.

In contrast, the dynamic nature of the exponential filter is beneficial in this area. It should be noted that the overall metrics of the whole Philippine site do not match this sample area, as there are far more significant areas of missed TP from the exponential filter from prolonged floods (further discussed below).
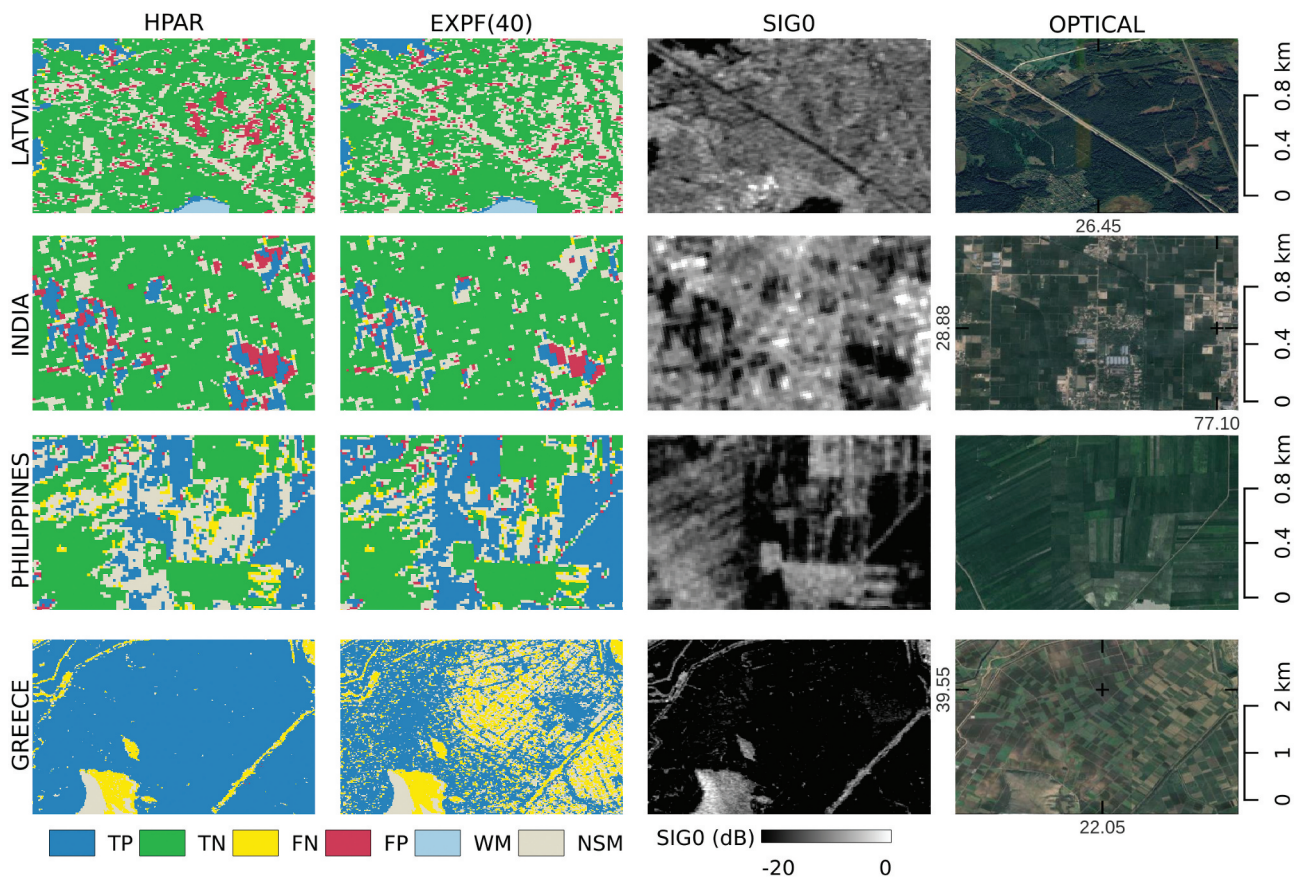
Figure 10. Flood confusion maps from Latvia (top row), India (2nd row), the Philippines (3rd row), and Greece (bottom row) study sites. Flood confusion maps from flood maps using harmonic model (left most column) versus exponential filter at *T*=40 (2nd column) with the flooded SIG0 backscatter (3rd column) and optical image from google as reference. Legend: FN - false negative, TN - true negative, TP - true positive, FP -false positive, WM - reference water mask, NSM - TU Wien no sensitivity mask.

5.4.3. Long floods

The test sites in Greece and the Philippines have lower exponential filter performance. We consider it consequential that these test sites were documented to have had prolonged floods (He et al. 2023; He et al. 2023). This points to a deficiency of the exponential filter in accurately modeling the no-flood reference probability distribution.

This results in underestimation at the Greece test site is highlighted in the bottom row of Figure 10. Prolonged flood results in lower backscatter estimates from the exponential filter; thus, the no-flood probability distribution moves closer to the flood probability distribution, causing conflicting distributions in some cases. As the exponential filter standard deviation was computed from the 2023 time series, we observed elevated variance which can be attributed to the prolonged floods in the area, thus exacerbating the underestimation issue.

6. Discussion

6.1. No-flood conditions

As expected, most of the increase in FPR at the tile level can be attributed to frozen soil (Baghdadi et al. 2018) and dry conditions (O'Grady, Leblanc, and Gillieson 2011) and dry conditions (O'Grady, Leblanc, and Gillieson 2011) supported by ERA5-Land data. Agricultural overestimation – unrelated to these conditions – which has been observed mostly on local scales (Bauer-Marschallinger et al. 2022; Cian et al. 2018) – we have now shown instances where they also cause a significant increase in FPR at the tile level.

Although the case of overestimation due to frozen soils and dry conditions could be effectively identified from auxiliary data (as is done in GFM (Matgen et al. 2022)), the effect of low backscatter due to agriculture is much more challenging to address due to local variations. Our analysis of FP frequency reveals that this overestimation is

influenced by the type of crops and cropping practices, as evidenced by plot-level variation. This observation suggests the possibility of seasonal and land cover class-based correction or reliability metric; thus, it is recommended for future work.

Although these overestimation issues in no-flood conditions were not completely eliminated, switching to an exponential filter-based no-flood reference improves overall performance. In most cases, the FPR of the exponential filter model is less than half of the harmonic model. We observed that the FPR differences between the harmonic model and the exponential filter is more pronounced in sites with clear seasonality. Temperate and arid regions benefit more compared to the tropical areas where there is no clear improvement.

In general, the FPR of the exponential model does not vary much based on T value. For several test cases, T values of 10 and 20 showed inconsistent results. There are instances where they have the lowest FPR but more often have the higher FPRs. Even on the tile level, all other T values were difficult to distinguish based on their performance FPR and RMSD values. Thus, to safely limit FPR in cases without flood, we suggest T values starting at 30.

The time series assessments were limited to the same Sentinel-1A relative orbit of the reference flood data to remove effects due to changing imaging geometry (Schlaffer et al. 2017). This means that for the 2023 time series per orbit, there were at most 30 samples per tile we analyzed. We recommend that a longer time-series analysis, e.g. two years, be conducted in the future. The flood time series and frequency analysis relies on the accuracy of the reference water mask (Rättich, Martinis, and Wieland 2020). The seven locations examined in this study do not exhibit substantial seasonally flooded regions; however, overlooking the possibility of localized genuine floods might result in the extent of false positives to be overstated (see Figure 7). Although we consider this a minor issue for the sites tested e.g. no big spikes in FPR in Slovenian case, we suggest using a higher quality and more consistent mask in future research.

6.2. Flood conditions

Based on CSI, UA, and PA values, the TU Wien flood mapping algorithm showed good performance relative to the reference flood maps for most of the seven validated flood events. The confusion maps presented mainly corroborated the quantitative trends of decreased FP from the exponential filter maps compared to the harmonic model maps.

We find a similar result of reduced overestimation with the exponential filter for the flooded scenes where reference flood maps were available. From the differences in the CSI, UA, and PA trends based on the values of T, we found that $T = 40$ is a good choice for most study sites. This selection corresponds to roughly nine Sentinel-1 observations and about four months in the temporal range. This criterion is similar to the common suggestion from literature to limit no-flood reference input to images near in time or season (Clement, Kilsby, and Moore 2018; Hostache, Matgen, and Wagner 2012).

Further, the computational needs for this number of input images seem reasonable, unlike higher T values which would be unmanageable at global scale. The number of input images appears consistent with suggestions of five images minimum (Karamvasis and Karathanassi 2021) as we see $T < = 20$ with less than five inputs having degraded performance. These qualitative trends are corroborated by confusion maps that point to the tested middle values T preferred over the lower and higher values. As the T value is less significant in the non-flooded scenes we select $T = 40$ as our default choice.

However, unlike in soil moisture studies where the T parameter has been well documented (Albergel et al. 2008; Paulik et al. 2014; Pellarin, Calvet, and Wagner 2006) and uses higher temporal resolution inputs, we can only use comparatively limited backscatter observations. Consequently, the number of observations used to make a no-flood estimate depends on the T value. Distinguishing the effect of the model independent of the number of observations is not possible from our experiments. Further, while care was taken to match reference flood maps to our results to minimize external differences (e.g. temporal and spatial mismatches), the reference data used are not actual ground truth. Thus, over- and under-detection due to the limitations of flood

retrievals from SAR backscatter are persistent in the analysis.

6.3. T-value selection

Based on the flooded and non-flooded test scenarios described previously, we have identified $T = 40$ as a reasonable selection based on several considerations. First, while most T values are quite similar, lower T values ($< = 20$) for specific test sites exhibited increased variance, prompting us to limit our range to $T > = 30$. Second, as shown in Figure 9, mid-range T values (40 to 90) present a more favorable pattern with less noise and less no-sensitivity pixels. Third, average metrics for flooded scenarios indicate a preference for $T = 40$. Finally, higher T values ($> = 90$) are computationally expensive, even for initializing the recursive formulation.

6.4. Long floods and exponential filter prospects

It is also clear that prolonged floods severely affect the performance no-flood references using the exponential filter model. While this issue is localized to pixels with longer floods and does not affect the overall performance in other regions a generalized solution is needed. A simple solution is to remove flooded Sentinel-1 images as inputs. However, the automated identification of images that contain floods is a significant scientific question on its own. Some workflows suggest using auxiliary markers, such as precipitation (Karamvasis and Karathanassi 2021), to omit dates with a high probability of being flooded. Another possibility is the removal of flooded scenes based on some (non-)similarity metric (Hostache, Matgen, and Wagner 2012). Although requiring significant infrastructure to execute, a recent method based on detecting time series anomalies by Fichtner et al. (2023) is currently being used in GFM, showing promising results.

From our results in section 5.1, there appears to be a potential to identify anomalies based on the ratios of the FPR and RMSD. There is often a good correlation between FPR and RMSD. When the FPR increases due to freezing soil conditions, a significant proportion of the area changes, meaning the RMSD also increases. In contrast, the increase in FPR due to dry

(and, to an extent, cropping practices) has a longer duration but proportional increase in RMSD.

Flood events appear as anomalies that do not follow this trend. Floods often cover a small portion of a 300 km-wide Equi7Grid T3 scene; hence, FPR does not increase much. Since RMSD is sensitive to outliers, a significant decrease in backscatter due to floods increases the RMSD even in cases where floods are relatively small. However, there seems to be inter-site variance; thus, it is unexplored here and left for future work.

7. Conclusions and outlook

In this study, we assessed the performance of different no-flood parameterizations of the TU Wien flood mapping algorithm using a novel non-flooded time-series approach and traditional qualitative and quantitative flood map assessments. We analyzed the algorithms performance on varying environmental and climatic zones for one year time-series. In doing so, we highlight spatiotemporal patterns of overestimation.

While the importance of a no-flood reference in SAR flood mapping algorithms has been extensively covered (Giustarini et al. 2013; Hostache, Matgen, and Wagner 2012; Li et al. 2018; Schlaffer et al. 2015; Zhao, Pelich, Hostache, Matgen, Wagner, & Chini, 2021), the impact it has on the overestimation of automatically classified non-flooded scenes has not been given attention until now. We find that flood overestimation at scale could be triggered not just by frost and dry soil conditions but also by agriculture. Further, the degree of agricultural overestimation depends on the crop type and agricultural practices.

Aside from limited testing we introduced in a previous work (Tupas et al. 2023a), to our knowledge this concept of testing flood mapping methods on non-flooded times series scenes have not yet been attempted before. This work sheds light on the frequency of these different overestimation issues, thus highlighting the need for further studies to reduce them.

We compared the original harmonic and novel exponential filter models with no-flood references, with the latter showing promising performance. Similar to observations from recent studies (Colacicco et al. 2024) the enhanced modeling of the no-flood reference resulted in improved flood maps. The exponential filter reduced overestimation in both

flooded and non-flooded conditions. This is supported by improved flood labeling in areas where dynamically updated no-flood models are required. Reduced overestimation by switching to the exponential filter can be complemented using topography-based priors (Tupas et al. 2023a), which improved the underestimation.

We found that the exponential filter with $T = 40$ provides a good balance in performance for both flooded and non-flooded conditions. This T value requires a reasonable time series input (allowing for application at a global scale) to achieve good initial results. However, the recursive formulation is still a must for actual NRT operations. Provided computational cost does not prohibit NRT application, more advanced updating of temporal models e.g. Kalman filters (Dalaison and Jolivet 2020; Komisarenko et al. 2022) should be explored.

Prolonged floods present an issue for the exponential filter based no-flood backscatter estimate and generated standard deviation, the two parameters needed to estimate the no-flood model probability distribution. Therefore, an automated screening of flooded Sentinel-1 images as input is strongly recommended for operational implementation both for the backscatter estimation and no-flood standard deviation calculation.

To conclude, we showed a holistic assessment of the TU Wien algorithm geared toward automated deployment over multiple climatic zones for flooded and non-flooded cases. As far as we are aware, analyses of flood mapping on this spatial and temporal extents have not been conducted previously. Understanding of the algorithm's limitations in the temporal and environmental context opens new avenues for improvement. While further development is needed, the exponential filter as a no-flood reference was shown to be a feasible alternative to the harmonic model. Overall, the exponential filter no-flood reference model shows great promise for improved global near-real-time flood mapping.

Abbrevations

BI	Bayes(ian) Inference
CEMS	Copernicus Emergency Management Service
CSI	Critical Success Index
DOY	Day Of Year
EODC	Earth Observation Data Centre for Water Resources Monitoring
EXPF	Exponential Filter
FN	False Negative
FP	False Positive
FPR	False Positive Rates
GFM	Global Flood Monitoring
HAND	Height Above Nearest Drainage
HPAR	Harmonic Parameters
NSM	No-sensitivity Mask
PA	Producer Accuracy
PDF	Probability Distribution Function
RMSD	Root Mean Square Deviation
UA	User Accuracy
NRT	Near-Real-Time
SAR	Synthetic Aperture Radar
SIG0	Sigma Nought backscatter coefficient σ_0
STD	Standard Deviation
TN	True Negative
TP	True Positive
WM	Water Mask

Disclosure statement

No potential conflict of interest was reported by the author(s).

ORCID

Mark Edwin Tupas http://orcid.org/0000-0002-8227-5299
Florian Roth http://orcid.org/0000-0002-8589-0182
Bernhard Bauer-Marschallinger http://orcid.org/0000-0001-7356-7516
Wolfgang Wagner http://orcid.org/0000-0001-7704-6857

Data availability statement

The data presented in this study are openly available at: https://doi.org/10.48436/3dd60-ydz51.

References

Albergel, C., C. Rüdiger, T. Pellarin, J.-C. Calvet, N. Fritz, F. Froissard, and E. Martin, A. Petitpa, B. Piguet, E. Martin. 2008. "From Near-Surface to Root-Zone Soil Moisture Using an Exponential Filter: An Assessment of the Method Based on in-Situ Observations and Model Simulations." *Hydrology and Earth System Sciences* 12 (6): 1323–1337. https://hess.copernicus.org/articles/12/1323/2008/ .

Alexandre, C., R. Johary, T. Catry, P. Mouquet, C. Révillion, S. Rakotondraompiana, and G. Pennober. 2020. "A Sentinel-1 Based Processing Chain for Detection of Cyclonic Flood Impacts." *Remote Sensing* 12 (2): 252. https://doi.org/10.3390/rs12020252.

Baghdadi, N., H. Bazzi, M. El Hajj, and M. Zribi. 2018. "Detection of Frozen Soil Using Sentinel-1 SAR Data." *Remote Sensing* 10 (8): 1182. https://doi.org/10.3390/rs10081182.

Barsi Kugler, Z., I. László, G. Szabó, H. M. Abdulmutalib, and H. M. Abdulmutalib. 2018. "Accuracy Dimensions In Remote Sensing." *International Archives of the Photogrammetry, Remote Sensing and Spatial Information Sciences* XLII-3:61–67. https://www.int-arch-photogramm-remote-sens-spatial-inf-sci.net/XLII-3/61/2018/.

Bauer-Marschallinger, B., S. Cao, M. E. Tupas, F. Roth, C. Navacchi, T. Melzer, and W. Wagner, W. Wagner. 2022. "Satellite-Based Flood Mapping Through Bayesian Inference from a Sentinel-1 SAR Datacube." *Remote Sensing* 14 (15): 3673. https://www.mdpi.com/2072-4292/14/15/3673 .

Bauer-Marschallinger, B., C. Paulik, S. Hochstöger, T. Mistelbauer, S. Modanesi, L. Ciabatta, and W. Wagner, L. Brocca, W. Wagner. 2018. "Soil Moisture from Fusion of Scatterometer and SAR: Closing the Scale Gap with Temporal Filtering." *Remote Sensing* 10 (7): 1030. https://www.mdpi.com/2072-4292/10/7/1030. (Number: 7 Publisher: Multidisciplinary Digital Publishing Institute).

Bauer-Marschallinger, B., D. Sabel, and W. Wagner. 2014. "Optimisation of Global Grids for High-Resolution Remote Sensing Data." *Computers & Geosciences* 72:84–93. https://doi.org/10.1016/j.cageo.2014.07.005.

Bezak, N., P. Panagos, L. Liakos, and M. Mikoš. 2023. "Brief Communication: A First Hydrological Investigation of Extreme August 2023 Floods in Slovenia, Europe." *Natural Hazards and Earth System Sciences* 23 (12): 3885–3893. https://doi.org/10.5194/nhess-23-3885-2023.

Ceola, S., F. Laio, and A. Montanari. 2014. "Satellite Nighttime Lights Reveal Increasing Human Exposure to Floods Worldwide." *Geophysical Research Letters* 41 (20): 7184–7190. https://doi.org/10.1002/2014GL061859.

Chang, L., Y.-T. Chen, J.-H. Wang, and Y.-L. Chang. 2021. "Rice-Field Mapping with Sentinel-1A SAR Time-Series Data."

Remote Sensing 13 (1): 103. https://www.mdpi.com/2072-4292/13/1/103.

Chini, M., R. Hostache, L. Giustarini, and P. Matgen. 2017. "A Hierarchical Split-Based Approach for Parametric Thresholding of SAR Images: Flood Inundation as a Test Case." *IEEE Transactions on Geoscience & Remote Sensing* 55 (12): 6975–6988. https://doi.org/10.1109/TGRS.2017.2737664.

Cian, F., M. Marconcini, P. Ceccato, and C. Giupponi. 2018. "Flood Depth Estimation by Means of High-Resolution SAR Images and Lidar Data." *Natural Hazards and Earth System Sciences* 18 (11): 3063–3084. https://doi.org/10.5194/nhess-18-3063-2018.

Clement, M. A., C. G. Kilsby, and P. Moore. 2018. "Multi-Temporal Synthetic Aperture Radar Flood Mapping Using Change Detection." *Journal of Flood Risk Management* 11 (2): 152–168. https://doi.org/10.1111/jfr3.12303.

Colacicco, R., A. Refice, R. Nutricato, F. Bovenga, G. Caporusso, A. D'Addabbo, and D. Capolongo, F. P. Lovergine, D. O. Nitti, D. Capolongo. 2024. "High-Resolution Flood Monitoring Based on Advanced Statistical Modeling of Sentinel-1 Multi-Temporal Stacks." *Remote Sensing* 16 (2): 294. https://www.mdpi.com/2072-4292/16/2/294.

Dalaison, M., and R. Jolivet. 2020. "A Kalman Filter Time Series Analysis Method for InSAR." *Journal of Geophysical Research Solid Earth* 125 (7): e2019JB019150. https://doi.org/10.1029/2019JB019150.

d'Andrimont, R., A. Verhegghen, G. Lemoine, P. Kempeneers, M. Meroni, and M. van der Velde. 2021. "From Parcel to Continental Scale – a First European Crop Type Map Based on Sentinel-1 and LUCAS Copernicus in-Situ Observations." *Remote Sensing of Environment* 266:112708. https://doi.org/10.1016/j.rse.2021.112708.

DeVries, B., C. Huang, J. Armston, W. Huang, J. W. Jones, and M. W. Lang. 2020. "Rapid and Robust Monitoring of Flood Events Using Sentinel-1 and Landsat Data on the Google Earth Engine." *Remote Sensing of Environment* 240:111664. https://doi.org/10.1016/j.rse.2020.111664.

Dimitriou, E., A. Efstratiadis, I. Zotou, A. Papadopoulos, T. Iliopoulou, G.-K. Sakki, and D. Koutsoyiannis, E. Rozos, A. Koukouvinos, A. D. Koussis, N. Mamassis. 2024. "Post-Analysis of Daniel Extreme Flood Event in Thessaly, Central Greece: Practical Lessons and the Value of State-Of-The-Art Water-Monitoring Networks." *Water* 16 (7): 980. https://www.mdpi.com/2073-4441/16/7/980.

Fahrland, E. L. A. I. L., P. Jacob, H. Schrader, and H. Kahabka. 2020. "Copernicus Digital Elevation Model Product Handbook." In *Airbus Defence and Space—Intelligence*, Potsdam, Germany.

Fichtner, F., N. Mandery, M. Wieland, S. Groth, S. Martinis, and T. Riedlinger. 2023. "Time-Series Analysis of Sentinel-1/2 Data for Flood Detection Using a Discrete Global Grid System and Seasonal Decomposition." *International Journal of Applied Earth Observation and Geoinformation* 119:103329. https://doi.org/10.1016/j.jag.2023.103329.

Giustarini, L., R. Hostache, D. Kavetski, M. Chini, G. Corato, S. Schlaffer, and P. Matgen. 2016. "Probabilistic Flood

Mapping Using Synthetic Aperture Radar Data." *IEEE Transactions on Geoscience & Remote Sensing* 54 (12): 6958–6969. https://doi.org/10.1109/TGRS.2016.2592951.

Giustarini, L., R. Hostache, P. Matgen, G. J.-P. Schumann, P. Bates, and D. Mason. 2013. "A Change Detection Approach to Flood Mapping in Urban Areas Using TerraSAR-X." *IEEE Transactions on Geoscience & Remote Sensing* 51 (4): 2417–2430. https://doi.org/10.1109/TGRS.2012.2210901.

Gorelick, N., M. Hancher, M. Dixon, S. Ilyushchenko, D. Thau, and R. Moore. 2017. "Google Earth Engine: Planetary-Scale Geospatial Analysis for Everyone." *Remote Sensing of Environment* 202:18–27. https://doi.org/10.1016/j.rse.2017.06.031.

Graham, E., D. Smart, S. H. Lee, D. Harris, A. Sibley, and D. Holley. 2023. "An Atmospheric River and a Quasi-Stationary Front Lead to Heavy Rainfall and Flooding Over Scotland, 6–8 October 2023." *Weather* 78 (12): 340–343. https://onlinelibrary.wiley.com/doi/abs/10.1002/wea.4501.

Grimaldi, S., J. Xu, Y. Li, V. R. N. Pauwels, and J. P. Walker. 2020. "Flood Mapping Under Vegetation Using Single SAR Acquisitions." *Remote Sensing of Environment* 237:111582. https://doi.org/10.1016/j.rse.2019.111582.

Gutierrez, M. A., N. M. Paguirigan, J. Raviz, M. R. Mabalay, E. Alosnos, L. Villano, S. Asilo, A. Arocena Jr., J. Maloom, and A. Laborte. 2019. "The Rice Planting Window in the Philippines: An Analysis Using Multi-temporal Sar Imagery." *International Archives of the Photogrammetry, Remote Sensing and Spatial Information Sciences* 4 (W19): 241–248. https://doi.org/10.5194/isprs-archives-XLII-4-W19-241-2019.

Harfenmeister, K., D. Spengler, and C. Weltzien. 2019. "Analyzing Temporal and Spatial Characteristics of Crop Parameters Using Sentinel-1 Backscatter Data." *Remote Sensing* 11 (13): 1569. https://doi.org/10.3390/rs11131569.

He, J., Q. Li, P.-W. Chan, C.-W. Choy, B. Mak, C.-C. Lam, and H.-Y. Luo. 2023. "An Observational Study of Typhoon Talim Over the Northern Part of the South China Sea in July 2023." *Atmosphere* 14 (9): 1340. https://doi.org/10.3390/atmos14091340.

He, K., Q. Yang, X. Shen, E. Dimitriou, A. Mentzafou, C. Papadaki, and E. N. Anagnostou. 2023. "Brief Communication: Storm Daniel Flood Impact in Greece 2023: Mapping Crop and Livestock Exposure from SAR." *Natural Hazards and Earth System Sciences Discussions* 1–16. Retrieved2024-02-11, from https://nhess.copernicus.org/preprints/nhess-2023-173/(Publisher:.CopernicusGmbH.

Hostache, R., P. Matgen, and W. Wagner. 2012. "Change Detection Approaches for Flood Extent Mapping: How to Select the Most Adequate Reference Image from Online Archives?" *International Journal of Applied Earth Observation and Geoinformation* 19:205–213. https://doi.org/10.1016/j.jag.2012.05.003.

Joubert-Boitat, I., A. Wania, and S. Dalmasso. 2020. *"Manual for CEMS-Rapid Mapping Products."* Accessed November 19, 2023, from https://publications.jrc.ec.europa.eu/repository/handle/JRC121741.

Kaku, K. 2019. "Satellite Remote Sensing for Disaster Management Support: A Holistic and Staged Approach Based on Case Studies in Sentinel Asia." *International Journal of Disaster Risk Reduction* 33:417–432. https://doi.org/10.1016/j.ijdrr.2018.09.015.

Karamvasis, K., and V. Karathanassi. 2021. "FLOMPY: An Open-Source Toolbox for Floodwater Mapping Using Sentinel-1 Intensity Time Series." *Water* 13 (21): 2943. https://doi.org/10.3390/w13212943.

Katiyar, V., N. Tamkuan, and M. Nagai. 2021. "Near-Real-Time Flood Mapping Using Off-The-Shelf Models with SAR Imagery and Deep Learning." *Remote Sensing* 13 (12): 2334. https://doi.org/10.3390/rs13122334.

Komisarenko, V., K. Voormansik, R. Elshawi, and S. Sakr. 2022. "Exploiting Time Series of Sentinel-1 and Sentinel-2 to Detect Grassland Mowing Events Using Deep Learning with Reject Region." *Scientific Reports* 12 (1): 983. https://doi.org/10.1038/s41598-022-04932-6.

Landuyt, L., A. V. Wesemael, G. J. Schumann, R. Hostache, N. E. C. Verhoest, and E. M. B. V. Coillie. 2019. "Flood Mapping Based on Synthetic Aperture Radar: An Assessment of Established Approaches." *IEEE Transactions on Geoscience & Remote Sensing* 57 (2): 722–739. https://doi.org/10.1109/TGRS.2018.2860054.

Lee, J.-S. 1983. "Digital Image Smoothing and the Sigma Filter." *Computer Vision, Graphics and Image Processing* 24 (2): 255–269. https://doi.org/10.1016/0734-189X(83)90047-6.

Lee, J.-S., J.-H. Wen, T. Ainsworth, K.-S. Chen, and A. Chen. 2009. "Improved Sigma Filter for Speckle Filtering of SAR Imagery." *IEEE Transactions on Geoscience & Remote Sensing* 47 (1): 202–213. https://doi.org/10.1109/TGRS.2008.2002881.

Li, Y., S. Martinis, S. Plank, and R. Ludwig. 2018. "An Automatic Change Detection Approach for Rapid Flood Mapping in Sentinel-1 SAR Data." *International Journal of Applied Earth Observation and Geoinformation* 73:123–135. https://doi.org/10.1016/j.jag.2018.05.023.

Lin, Y., S.-H. Yun, A. Bhardwaj, and E. Hill. 2019. "Urban Flood Detection with Sentinel-1Multi-Temporal Synthetic Aperture Radar (SAR) Observations in a Bayesian Framework: A Case Study for Hurricane Matthew." *Remote Sensing* 11 (15): 1778. https://doi.org/10.3390/rs11151778.

Mabalay, M. R., J. Raviz, E. Alosnos, M. Barbieri, E. Quicho, J. E. A. Bibar, and A. Laborte. 2022. "The Philippine Rice Information System (PriSM)philippine Rice Information System (PRISM): An Operational MonitoringMonitoring and Information System on RiceRicephilippine Rice Information System (Prism)monitoring." In *Remote Sensing of Agriculture and Land Cover/Land Use Changes in South and Southeast Asian Countries*, edited by K. P. Vadrevu, T. Le Toan, S. S. Ray, and C. Justice, 133–150. Cham: Springer International Publishing. https://doi.org/10.1007/978-3-030-92365-57.

Maity, S., C. Patnaik, M. Chakraborty, and S. Panigrahy. 2004. "Analysis of Temporal Backscattering of Cotton Crops Using a Semiempirical Model." *IEEE Transactions on Geoscience & Remote Sensing* 42 (3): 577–587. https://doi.org/10.1109/TGRS.2003.821888.

Martinis, S., J. Kersten, and A. Twele. 2015. "A Fully Automated TerraSAR-X Based Flood Service." *Isprs Journal of Photogrammetry & Remote Sensing* 104:203–212. https://doi.org/10.1016/j.isprsjprs.2014.07.014.

Martinis, S., A. Twele, and S. Voigt. 2009. "Towards Operational Near Real-Time Flood Detection Using a Split-Based Automatic Thresholding Procedure on High Resolution TerraSAR-X Data." *Natural Hazards and Earth System Sciences* 9 (2): 303–314. https://doi.org/10.5194/nhess-9-303-2009.

Matgen, P., M. Chini, B. Bauer-Marschallinger, F. Roth, C. Krullikowski, C. W. Y. Chow, and M. Seewald. 2022. "Provision of an Automated, Global, Satellite-Based Flood Monitoring Product for the Copernicus Emergency Management Service: Product Definition Document (PDD) [Monograph]." Accessed March 12, 2024, from https://extwiki.eodc.eu/GFM/PDD. (Num Pages: 75).

Metzger, M. J. 2018. *The Global Environmental Stratification: A High-Resolution Bioclimate Map of the World*. The University of Edinburgh. https://datashare.ed.ac.uk/handle/10283/3089.

Muñoz-Sabater, J., E. Dutra, A. Agustí-Panareda, C. Albergel, G. Arduini, G. Balsamo, and J.-N. Thépaut, M. Choulga, S. Harrigan, H. Hersbach, B. Martens. 2021. "ERA5-Land: A State-Of-The-Art Global Reanalysis Dataset for Land Applications." *Earth System Science Data* 13 (9): 4349–4383. https://essd.copernicus.org/articles/13/4349/2021/.

Nagai, H., T. Abe, and M. Ohki. 2021. "SAR-Based Flood Monitoring for Flatland with Frequently Fluctuating Water Surfaces: Proposal for the Normalized Backscatter Amplitude Difference Index (NoBADI)." *Remote Sensing* 13 (20): 4136. https://doi.org/10.3390/rs13204136.

O'Grady, D., M. Leblanc, and D. Gillieson. 2011. "Use of ENVISAT ASAR Global Monitoring Mode to Complement Optical Data in the Mapping of Rapid Broad-Scale Flooding in Pakistan." *Hydrology and Earth System Sciences* 15 (11): 3475–3494. https://doi.org/10.5194/hess-15-3475-2011.

Paulik, C., W. Dorigo, W. Wagner, and R. Kidd. 2014. "Validation of the ASCAT Soil Water Index Using in situ Data from the International Soil Moisture Network." *International Journal of Applied Earth Observation and Geoinformation* 30:1–8. https://doi.org/10.1016/j.jag.2014.01.007.

Pelich, R., M. Chini, R. Hostache, P. Matgen, J. M. Delgado, and G. Sabatino. 2017. "Towards a Global Flood Frequency Map from SAR Data." In *2017 IEEE International Geoscience and Remote Sensing Symposium (IGARSS)*, Fort Worth, Texas, USA, July 23–28, 2017, 4024–4027.

Pellarin, T., J.-C. Calvet, and W. Wagner. 2006. "Evaluation of ERS Scatterometer Soil Moisture Products Over a Half-Degree Region in Southwestern France." *Geophysical Research Letters* 33 (17). https://onlinelibrary.wiley.com/doi/abs/10.1029/2006GL027231.

Pratt, J. W. 1959. "Remarks on Zeros and Ties in the Wilcoxon Signed Rank Procedures." *Journal of the American Statistical Association* 54 (287): 655–667. https://doi.org/10.1080/01621459.1959.10501526.

Rättich, M., S. Martinis, and M. Wieland. 2020. "Automatic Flood Duration Estimation Based on Multi-Sensor Satellite Data." *Remote Sensing* 12 (4): 643. https://doi.org/10.3390/rs12040643.

Refice, A., D. Capolongo, G. Pasquariello, A. D'Addabbo, F. Bovenga, R. Nutricato, and L. Pietranera. 2014. "SAR and InSAR for Flood Monitoring: Examples with COSMO-Skymed Data." *IEEE Journal of Selected Topics in Applied Earth Observations & Remote Sensing* 7 (7): 2711–2722. https://doi.org/10.1109/JSTARS.2014.2305165.

Refice, A., A. D'Addabbo, F. Lovergine, F. Bovenga, R. Nutricato, and D. Nitti. 2022. "Improving Flood Monitoring Through Advanced Modeling of Sentinel-1 Multi-Temporal Stacks." In *IGARSS 2022 - 2022 IEEE International Geoscience and Remote Sensing Symposium*, 5881–5884. https://ieeexplore.ieee.org/document/9883943.

Rentschler, J., M. Salhab, and B. A. Jafino. 2022. "Flood Exposure and Poverty in 188 Countries." *Nature Communications* 13 (1): 3527. https://doi.org/10.1038/s41467-022-30727-4.

Salamon, P., N. Mctlormick, C. Reimer, T. Clarke, B. Bauer-Marschallinger, W. Wagner, and A. Walli. 2021. "The New, Systematic Global Flood Monitoring Product of the Copernicus Emergency Management Service." In *2021 IEEE International Geoscience and Remote Sensing Symposium IGARSS*, Virtual Symposium, Brussels, Belgium, July 12–16, 2021, 1053–1056.

Schlaffer, S., M. Chini, L. Giustarini, and P. Matgen. 2017. "Probabilistic Mapping of Flood-Induced Backscatter Changes in SAR Time Series." *International Journal of Applied Earth Observation and Geoinformation* 56:77–87. https://doi.org/10.1016/j.jag.2016.12.003.

Schlaffer, S., P. Matgen, M. Hollaus, and W. Wagner. 2015. "Flood Detection from Multi-Temporal SAR Data Using Harmonic Analysis and Change Detection." *International Journal of Applied Earth Observation and Geoinformation* 38:15–24. https://doi.org/10.1016/j.jag.2014.12.001.

Schumann, G., L. Giustarini, A. Tarpanelli, B. Jarihani, and S. Martinis. 2023. "Flood Modeling and Prediction Using Earth Observation Data." *Surveys in Geophysics* 44 (5): 1553–1578. https://doi.org/10.1007/s10712-022-09751-y.

Shen, X., E. N. Anagnostou, G. H. Allen, G. Robert Brakenridge, and A. J. Kettner. 2019. "Near-Real-Time Non-Obstructed Flood Inundation Mapping Using Synthetic Aperture Radar." *Remote Sensing of Environment* 221:302–315. https://doi.org/10.1016/j.rse.2018.11.008.

Sherpa, S. F., M. Shirzaei, C. Ojha, S. Werth, and R. Hostache. 2020. "Probabilistic Mapping of August 2018 Flood of Kerala, India, Using Space-Borne Synthetic Aperture Radar." *IEEE Journal of Selected Topics in Applied Earth Observations & Remote Sensing* 13:896–913. https://doi.org/10.1109/JSTARS.2020.2970337.

Stephens, E., G. Schumann, and P. Bates. 2014. "Problems with Binary Pattern Measures for Flood Model Evaluation." *Hydrological Processes* 28 (18): 4928–4937. https://doi.org/10.1002/hyp.9979.

Tarasova, L., D. Lun, R. Merz, G. Blöschl, S. Basso, M. Bertola, and R. Kumar, O. Rakovec, L. Samaniego, S. Thober, R. Kumar.

2023. "Shifts in Flood Generation Processes Exacerbate Regional Flood Anomalies in Europe." *Communications Earth & Environment* 4 (1): 1–12. https://www.nature.com/articles/s43247-023-00714-8.

Tarpanelli, A., A. C. Mondini, and S. Camici. 2022. "Effectiveness of Sentinel-1 and Sentinel-2 for Flood Detection Assessment in Europe." *Natural Hazards and Earth System Sciences* 22 (8): 2473–2489. https://doi.org/10.5194/nhess-22-2473-2022.

Tellman, B., J. A. Sullivan, C. Kuhn, A. J. Kettner, C. S. Doyle, G. R. Brakenridge, and D. A. Slayback, D. A. Slayback. 2021. "Satellite Imaging Reveals Increased Proportion of Population Exposed to Floods." *Nature* 596 (7870): 80–86. https://www.nature.com/articles/s41586-021-03695-w.

Torres, R., P. Snoeij, D. Geudtner, D. Bibby, M. Davidson, E. Attema, and F. Rostan, B. Rommen, N. Floury, M. Brown, I. N. Traver. 2012. "GMES Sentinel-1 Mission." *Remote Sensing of Environment* 120:9–24. https://www.sciencedirect.com/science/article/pii/S0034425712000600.

Tupas, M. E., F. Roth, B. Bauer-Marschallinger, and W. Wagner. 2023a. "Improving Sentinel-1 Flood Maps Using a Topographic Index as Prior in Bayesian Inference." *Water* 15 (23): 4034. https://doi.org/10.3390/w15234034.

Tupas, M. E., F. Roth, B. Bauer-Marschallinger, and W. Wagner. 2023b. "An Intercomparison of Sentinel-1 Based Change Detection Algorithms for Flood Mapping." *Remote Sensing* 15 (5): 1200. https://doi.org/10.3390/rs15051200.

Tupas, M., C. Navacchi, F. Roth, B. Bauer-Marschallinger, F. Reuß, and W. Wagner. 2022. "COmputing Global Harmonic Parameters For Flood Mapping Using Tu Wien's Sar Datacube Software Stack." In *The International Archives of the Photogrammetry, Remote Sensing and Spatial Information Sciences*, 495–502. Vol. XLVIII-4-W1-2022. Copernicus GmbH. https://www.int-arch-photogramm-remote-sens-spatial-inf-sci.net/XLVIII-4-W1-2022/495/2022/.

Twele, A., W. Cao, S. Plank, and S. Martinis. 2016. "Sentinel-1-Based Flood Mapping: A Fully Automated Processing Chain." *International Journal of Remote Sensing* 37 (13): 2990–3004. https://doi.org/10.1080/01431161.2016.1192304.

Ulaby, F. T., G. A. Bradley, and M. C. Dobson. 1979. "Microwave Backscatter Dependence on Surface Roughness, Soil Moisture, and Soil Texture: Part II-Vegetation-Covered Soil." *IEEE Transactions on Geoscience Electronics* 17 (2): 33–40. https://doi.org/10.1109/TGE.1979.294626.

Ulloa, N., S.-H. Chiang, and S.-H. Yun. 2020. "Flood Proxy Mapping with Normalized Difference Sigma-Naught Index and Shannon's Entropy." *Remote Sensing* 12 (9): 1384. https://doi.org/10.3390/rs12091384.

Vreugdenhil, M., W. Wagner, B. Bauer-Marschallinger, I. Pfeil, I. Teubner, C. Rüdiger, and P. Strauss. 2018. "Sensitivity of Sentinel-1 Backscatter to Vegetation Dynamics: An Austrian Case Study." *Remote Sensing* 10 (9): 1396. https://doi.org/10.3390/rs10091396.

Wagner, W., B. Bauer-Marschallinger, C. Navacchi, F. Reuß, S. Cao, C. Reimer, and C. Briese. 2021. "A Sentinel-1 Backscatter Datacube for Global Land Monitoring Applications." *Remote Sensing* 13 (22): 4622. https://doi.org/10.3390/rs13224622.

Wagner, W., G. Lemoine, and H. Rott. 1999. "A Method for Estimating Soil Moisture from ERS Scatterometer and Soil Data." *Remote Sensing of Environment* 70 (2): 191–207. https://doi.org/10.1016/S0034-4257(99)00036-X.

Wagner, W., R. Lindorfer, S. Hahn, H. Kim, M. Vreugdenhil, A. Gruber, and M. Trnka, M. Trnka. 2024. "Global Scale Mapping of Subsurface Scattering Signals Impacting ASCAT Soil Moisture Retrievals." *IEEE Transactions on Geoscience & Remote Sensing* 62:1–20. https://ieeexplore.ieee.org/document/10601171?source=.

Westerhoff, R. S., M. P. H. Kleuskens, H. C. Winsemius, H. J. Huizinga, G. R. Brakenridge, and C. Bishop. 2013. "Automated Global Water Mapping Based on Wide-Swath Orbital Synthetic-Aperture Radar." *Hydrology and Earth System Sciences* 17 (2): 651–663. https://doi.org/10.5194/hess-17-651-2013.

Wieland, M., and S. Martinis. 2019. "A Modular Processing Chain for Automated Flood Monitoring from Multi-Spectral Satellite Data." *Remote Sensing* 11 (19): 2330. https://doi.org/10.3390/rs11192330.

Wilcoxon, F. 1945. "Individual Comparisons by Ranking Methods." *Biometrics Bulletin* 1 (6): 80–83. https://doi.org/10.2307/3001968.

Wu, X., Z. Zhang, S. Xiong, W. Zhang, J. Tang, Z. Li, and R. Li. 2023. "A Near-Real-Time Flood Detection Method Based on Deep Learning and SAR Images." *Remote Sensing* 15 (8): 2046. https://www.mdpi.com/2072-4292/15/8/2046.

Zanaga, D., R. Van De Kerchove, W. De Keersmaecker, N. Souverijns, C. Brockmann, R. Quast, and O. Arino. 2021. "ESA WorldCover 10 M 2020 V100, Zenodo." Accessed March 14, 2024, from https://zenodo.org/records/5571936 .

Zhao, J., R. Pelich, R. Hostache, P. Matgen, S. Cao, W. Wagner, and M. Chini. 2021. "Deriving Exclusion Maps from C-Band SAR Time-Series in Support of Floodwater Mapping." *Remote Sensing of Environment* 265:112668. https://doi.org/10.1016/j.rse.2021.112668.

Zhao, J., R. Pelich, R. Hostache, P. Matgen, W. Wagner, and M. Chini. 2021. "A Large-Scale 2005–2012 Flood Map Record Derived from ENVISAT-ASAR Data: United Kingdom as a Test Case." *Remote Sensing of Environment* 256:112338. https://doi.org/10.1016/j.rse.2021.112338.